ISBN 978-82-326-0310-7 (printed version)
ISBN 978-82-326-0311-4 (electronic version)
ISSN 1503-8181

NTNU – Trondheim
Norwegian University of
Science and Technology

Afshin Abbasi Hoseini

Doctoral Thesis

Doctoral theses at NTNU, 2014:194

Afshin Abbasi Hoseini

Experimental study of turbulent flow with dispersed rod-like particles through optical measurements

NTNU
Norwegian University of Science and Technology
Faculty of Engineering Science and Technology
Department of Energy and Process Engineering

NTNU – Trondheim
Norwegian University of
Science and Technology

Doctoral theses at NTNU, 2014:194

NTNU

Afshin Abbasi Hoseini

Experimental study of turbulent flow with dispersed rod-like particles through optical measurements

Thesis for the degree of Philosophiae Doctor

Trondheim, June 2014

Norwegian University of Science and Technology
Faculty of Engineering Science and Technology
Department of Energy and Process Engineering

NTNU – Trondheim
Norwegian University of
Science and Technology

NTNU
Norwegian University of Science and Technology

Thesis for the degree of Philosophiae Doctor

Faculty of Engineering Science and Technology
Department of Energy and Process Engineering

ISBN 978-82-326-0310-7 (printed version)
ISBN 978-82-326-0311-4 (electronic version)
ISSN 1503-8181

Doctoral theses at NTNU, 2014:194

Printed by Skipnes Kommunikasjon as

“You must take the life the way it comes at you and make the best of it.”

Life of Pi, Yann Martel

CONTENTS

PREFACE

This PhD dissertation is apparently submitted to describe the authentically performed investigations during a period from February 2010 to March 2014 at Norwegian University of Science and Technology (NTNU), Faculty of Engineering Science and Technology, Department of Energy and Process Engineering. The Norwegian Research Council has provided the main financial support (project number of 191201/F20). The experiments were carried out at Linné FLOW Centre, KTH Mechanics, Royal Institute of Technology (KTH), Stockholm, Sweden. COST (European Cooperation in Science and Technology) Action FP1005 financed my short-term scientific mission at KTH.

Trondheim, June 2014

Afshinah Abbasi Hoseini

Acknowledgments

I would like to express my appreciation to my supervisor, Professor Helge Andersson, who granted me the opportunity, inspiration, courage and support. He provided me with the ultimate freedom that a researcher could possibly face for conducting a work along the track of interest and enthusiasm.

I owe a debt of gratitude to Associate Professor Fredrik Lundell, whose warm welcome to his lab prepared the ground for achieving the greatest wish of my life. Our challenging discussions gave me the opportunity to advance my knowledge and perfect my research and engineering skills.

I would also like to thank my colleague, Dr. Mustafa Barri, Dr. Lihao Zhao, Christofer Nilsen and Niranjan Challabotla from the Department of Energy and Process Engineering, NTNU. It was a pleasure for me to work with you. In addition, during my visit at Linné FLOW Centre in KTH, I have had the opportunity to cooperate with many people for which I am grateful. Karl Håkansson and Mathias Kvick helped me a lot with the working of the experimental setup and steerable filter for detection of fiber images in visualizations. I also am glad to acknowledge Ramin Imani Jajarmi's contribution to overcome the challenges during my experiments. All NTNU technical and administrative staffs are appreciated for their helps and supports.

Personally, I should say that four years far away from hometown have been a long time, and it would not have been possible for me to this without the friendship and company of the friends I have found in Norway. My special thanks go to my friends who know their name is carved on my heart.

Besides, the greatest thanks of all I owe to my family in Iran, my mother and father, my siblings, my uncles and aunt for their unlimited support and their encouragements throughout my life. I never forget Farahnaz, Morad and Faranak whom I have had the most enjoyable time of my life with them.

Finally, my wife, Fatemeh Zeinali, deserves the special mention for her unconditional love and being always with me, but words fail me to express my deepest gratitude to her. Only I can say, "I love you".

Summary

The knowledge of the behavior of non-spherical particles suspended in turbulent flows covers a wide range of applications in engineering and science. Dispersed two-phase flows and turbulence are the most challenging subjects in engineering, and when combined it gives rise to more complexities as the result of the inherent stochastic nature of the turbulence of the carrier-phase together with the random distribution of the dispersed phase. Moreover, for anisotropic particles the coupling between the translation and rotation of particle increases the complication. Because of the practical importance of prolate particle-laden turbulent flows, the plenty of numerical and experimental works have been conducted to study such suspensions.

Numerical approaches have given valuable insight of turbulent suspension flows, although the computation has been only carried out at the macro scale and models, not including flow distortion around the particle, comprise the detail of the flow in the order of a particle size. In addition, the model of the forces imposed on the particle by the fluid and mass point treatment are strictly valid for infinitely small particle having size less than all scales of the fluid turbulence. Fully resolved solution at the scale of the dispersed phase in turbulent flows for high Reynolds number has been recently performed but is still a challenge.

On the other hand, the presence of particle as the dispersed phase makes experimental measurements much more complicated than those with single phase as a result of particles interference. The area of considerable difficulty with this type of experiments is the measurement of the fluid-phase velocity remarkably close to the particle surface. Generally, experimental researches have been concentrated on measuring the mean velocity and Reynolds stresses of the carrier-phase, and the mean velocity, fluctuations, orientation and accumulation of the non-spherical particles. Higher-order quantities, including Lagrangian particle velocity correlations, the carrier-phase turbulence modulation, and two-particle and particle-fluid velocity correlations are also of interest.

It has been found that the rotational and translational movements of the fiber-shaped particle depend on the nature of carrier-phase field and fiber characteristics such as aspect ratio, fiber Stokes number, fiber Reynolds number, and the ratio of fiber to flow length scale.

With the development of PIV (Particle Image Velocimetry) and PTV (Particle Tracking Velocimetry) techniques, it has been appeared that combined PIV/PTV will be the best available choice for the experimental study of dispersed two-phase flows. The purpose of combined PIV/PTV measurement of two-phase systems is simultaneous measurements of fluid and suspended objects, where the PIV measurement of the fluid phase are combined with PTV measurement of the dispersed phase.

The objective of this doctoral thesis is to study the behavior of rod-like particles suspended in wall-bounded turbulent flow through simultaneous PIV/PTV measurements of the velocity of the flow field and particle motion. As a representative of rod-like particles, I have employed cellulose acetate fibers with the length to diameter ratio (aspect ratio) larger than one. Here, It has been considered only dilute suspensions with no flocculation; thus fiber-fiber interaction is negligible. The measurements have been conducted within the parallel planes (2D view) illuminated by laser in the streamwise direction in thin film suspension flowing on the water table setup at Linné FLOW Centre, KTH Mechanics Lab. It is shown that this setup is a well-behaved experimental model of half channel flows often used in Direct Numerical Simulation (DNS) investigations. Therefore, the experimental results are comparable to their DNS counterpart where it is convenient. A single camera PIV technique has been used to measure flowing suspension. Therefore, it has been needed to preprocess images using a spatial median filter to separate images of two phases, tracer particles as representative of fluid and fibers suspended. The well-known PIV processing algorithms have been applied to the phase of fluid. I have also introduced a novel algorithm to recognize and match fibers in consecutive images to track fibers and estimate their velocity.

It is not feasible to study all relevant aspects of particle-laden turbulent flows in a single study. In this study, I present the statistics of the rotational and translational motion of fiber-like particles and the surrounding fluid velocity. To the author's knowledge, remarkably little experimental work has been published to date on simultaneous measurement of fiber motion and turbulence field in a turbulent fiber suspension flow to reveal dynamics of fibers in this regime. Therefore, the results of this work will be profitable in better understanding of such multiphase flows. The statistical analysis of the translational motion of fibers shows that the size of fiber is a significant factor for the dynamical behavior of the fiber near the wall. It has been observed that, in the region near the wall, the probability of presence of the long fibers is high in both the high-speed and low-speed streaks of flow, and the mean velocity of fibers almost conforms to the mean velocity of flow; whereas the short fibers are mostly present in the low-speed areas, and the fiber mean velocity obey the dominant flow velocity in these areas. In the far-wall

regions, the translation of fibers is practically unaffected by the aspect ratio, whereas it depends crucially on the wall-normal distance. Moreover, it was found that in the case of long fibers near the wall, the low speed fibers mostly are orientated in streamwise direction. On the other hand, there is no preferential orientation for fast long fibers. Although wall-normal velocities were not measured in this study, it is hypothesized that this behavior is a result of fibers being affected by the sweep and ejection events known to occur in wall-bounded turbulent flow. The fast fibers are in sweep environment and comes from the upper layer. The low speed fibers are into ejection areas in the vicinity of the wall, and the wall has a stabilizing effect on them. The short fibers are still oriented mostly in streamwise direction for a certain range of low velocity. Furthermore, since a considerable change of the fiber behavior is observed in a certain ratio of the fiber length to the fiber distance from the solid wall, it is supposed that this ratio is also a prominent parameter for the behavior of fiber near the wall.

The results presented are in terms of viscous wall units wherever are denoted by superscript "+".

Chapter 1

INTRODUCTION

Dispersed two-phase flows happen commonly in many engineering and science applications, and they are often turbulent. These flows are characterized by a phase dispersed in the form of solid particle, droplet, or bubble within a fluid (gas or liquid) as carrier phase. Processes such as droplet or bubble break-up or particle agglomeration indeed change the interface between the phases. However, dispersed multiphase flows are distinguished from other types of multiphase flows, where the interface between the dispersed and carrier phases is considered in terms of particle-size spectra without the detailed evolution of the interface. Dispersed two-phase flows and turbulence are two of the most challenging issues in fluid mechanics, and when come together it leads to being further complicated because of the inherent stochastic nature of the turbulence of the carrier-phase together with the random distribution of the dispersed phase. Moreover, for non-spherical particles the coupling between the translation and rotation of particle increases the complexity.

1. Applications

In the following, examples involving two-phase flows with suspended particles are outlined to illustrate the wide application of such flows in the industry and science. In plenty of conditions, the particles have a non-spherical shape, and the flow is turbulent.

1.1. Cyclone separator

The separating of substances in the form of particle and droplet from industrial fluid is an important application of fluid-particle/droplet flows. Several methods are employed to remove particles or droplets from the flow. If the particles are sufficiently large, a settling chamber can be used in which the condensed impurities simply depart the flowing gas or liquid and are collected. For small particles into gas, the cyclone separator is used, Figure 1. The gas-particle flow enters the device in a tangential direction. The particles migrate toward the wall due to centrifugal acceleration and then fall toward the bottom where they are collected. The gases converge toward the center and form a vortex flow, which exit through a hatch on

the top. The performance of the cyclone is quantified by the particle size and density [1].

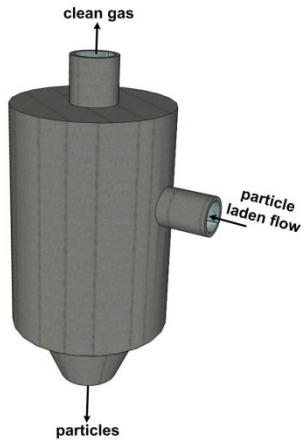

Figure 1 Cyclone separator;

1.2. Long distance material transport

Particle laden flows can be also seen in long distance transporting materials by either gases or liquids, depending on application.

The transport of materials by air is known as pneumatic transport, which is used widely in the industry for the transport of solid materials such as cement, grains, metal powders, ores, and coal. It has been particularly useful in layouts where obstacles prevent straight-line transport like conveyer belt or systems, which require tapping the line at arbitrary locations. Flow patterns depend on many factors, including particle loading, Reynolds number, particle properties and the layout of pipeline. Figures 2 illustrate the regimes that have been identified for gas-particle flows in a horizontal pipe. When the gas velocity is sufficiently high, the particles are well mixed and maintained in an almost homogeneous state by turbulent mixing, Figure 2.a. As the gas velocity is decreased, the particles begin to settle out and accumulate on the bottom of the pipe, and series of dunes begin to be formed due to the turbulent gas flow as depicted in Figure 2.b. The velocity in which deposition begins to occur in the pipe is called "the saltation velocity". As particles keep filling the pipe, there are alternate regions where particles have settled and where they are still in suspension. This is called slug flow, Figure 2.c. Finally, at lower gas velocities, the pipe is filled by particles, and the gas flows through a packed bed, shown in Figure 2.d. At this point, the particle transport is ceased. Pneumatic conveying systems are generally categorized in dilute and dense phase transport. Dilute-phase transport normally operates with low solids loading on low

pressure and high velocity. In dense phase transport, the pressure difference and solids loading are higher, but lower velocity, which leads to less material degradation and line erosion [1].

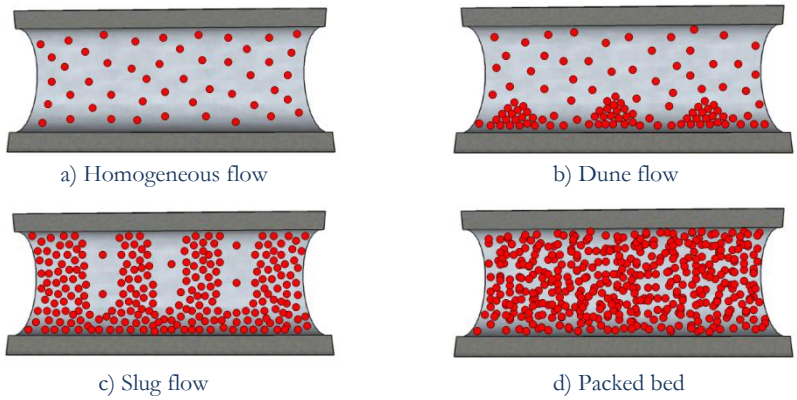

Figure 2 Horizontal pneumatic transport;

The transport of particles in liquids is identified as slurry flow. Drilling fluid is an example of this application. It is often used while drilling oil and natural gas wells to carry cuttings up to the surface. Its ability to do so depends on cutting size, shape, and density, and speed of fluid traveling up the well. The mechanics of the liquid-solid in slurry flow is complicated because of the particle-particle and fluid-particle interaction. Homogeneous slurries normally consist of small particles that are kept in suspension by the turbulence of the carrier fluid. Usually the homogeneous slurry is treated as a single-phase fluid with modified properties that depend on particle loading.

1.3. Solid propellant rocket

Another example is a gas-particle flow in a propulsion system of the solid propellant rocket. The fuel of solid propellant rocket can consist of aluminum powder. When the aluminum burns, small alumina droplets are produced and travel out the nozzle along with the exhaust gases, Figure 3. The presence of these particles decreases the propulsion of the rocket. The principles of gas-particle flows are used to design nozzles to achieve the best performance possible within the design constraints of the system.

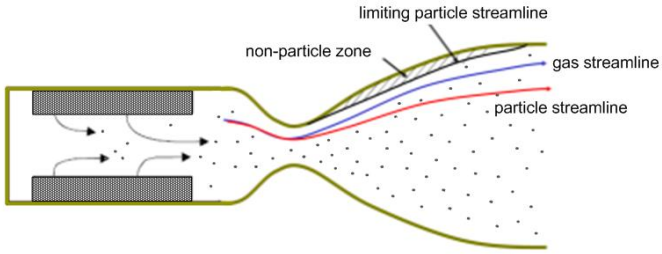

Figure 3 Solid propellant rocket motor;

1.4. Papermaking

Fiber-reinforced composites processing and paper manufacturing industry are of broad applications of multiphase flow process in which the relevant properties of the final product depend on the interaction between fluid and the fibers suspended. Although the phenomena happened throughout the process are not unique, fluid mechanics plays a key role in the final quality of the product.

For instance in the papermaking process, a dilute cellulose fiber suspension is jetted through a headbox, Figure 4. The headbox is the initial part of a paper machine, and its task is to deliver a thin spanwise homogeneous suspension onto the dewatering part, where the paper sheet is formed. The turbulent velocity profiles of fiber suspension can be characterized by a correlation with fiber concentration and Reynolds number as the main parameters. The acceleration of the flow in the contraction part influences both the fiber flocs and the fiber orientation in the final paper sheet. An additional aspect is the effect of the wall shear level on the fiber orientation [2].

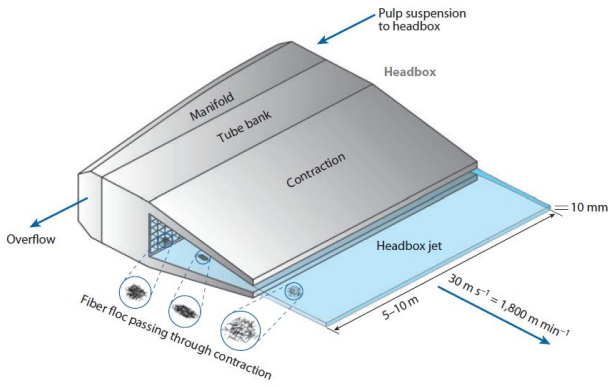

Figure 4 The schematic of a headbox [2], courtesy of L.D. Soderberg;

As shown in Figure 5, in the dewatering part a planar fiber suspension jet produced by the headbox impinges on a moving permeable wire belt (forming fabrics), so the water is drained through the belt and the fibers begin to form a network [2].

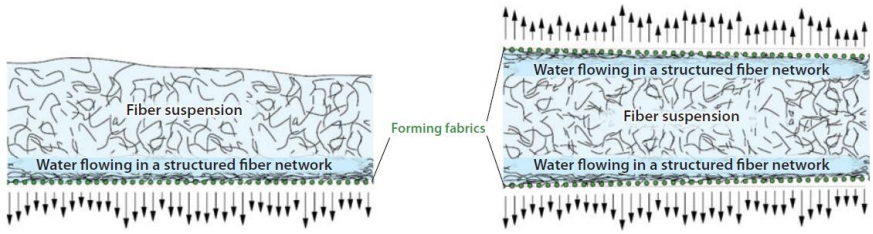

Figure 5 Dewatering and consolidating the fiber network on one wire (left) or between two wires (right) [2], courtesy of L.D. Soderberg;

1.5. Environmental fluid mechanics

In nature, we can also see particle-laden flows in the sandstorm, sedimentation of various substances in rivers, aerosols within the atmospheric boundary layer, and contaminant transport in the air and water. Therefore, the knowledge of particle transport, dispersion and accumulation processes in nature flows, from the micro scale to the planetary scale, provides a basis for the development of predictions and sustainable environmental management.

Figure 6 The sandstorm is an example of particles dispersed in atmospheric turbulent flow [picture: © Carters News Agency/Peter Vruggink];

For instance, the mechanism of particle drifting within the atmospheric boundary layer or rivers is widely found in phenomena surrounding us, including snowdrift on infrastructure such as roads, avalanche risk, soil erosion in farmland,

migration of dunes across deserts, and sedimentation in rivers. Although these examples involve different materials, the physics of mechanisms is similar. Depending on combinations of particle size and fluid velocity, large boulders creep along the surface; smaller particles hop and are entrained into downstream, and tiny sediments are transferred by the suspension flow. Typical trajectories of these three different transport modes can be divided into two layers, the suspension layer and saltation layer where also creeping movement occurs, as depicted in Figure 7.

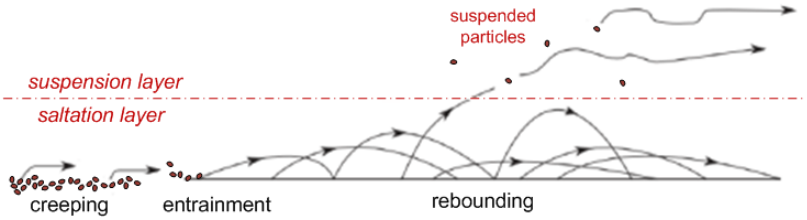

Figure 7 the three different behaviors of drifting particle within the turbulent boundary layer;

1.6. Particle-laden wall flows

The dynamics of a particle phase in wall bounded flows is crucial to predict failures of gas turbine blade, wind turbine blade, aircraft wing and etc accurately due to particle collision and deposition on the surface [3, 4].

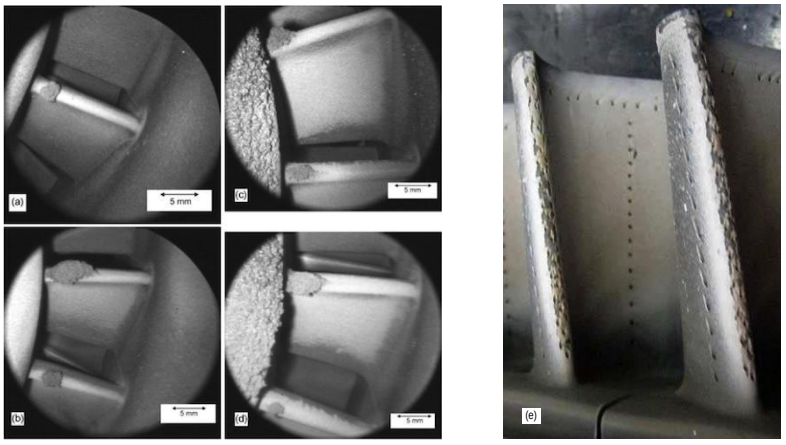

Figure 8 Volcanic ash deposits and erosion in a turbojet; (a) Fine particle size, minimal deposits; (b) Medium particle size, lumps of deposit on blades and combustion chamber wall; (c) Medium particle size, deposit covers more than 50% of combustion chamber wall; (d) Coarse particle size, deposition of leading edges of blades and combustion chamber wall deposits greater than 1 mm; (e) erosion of leading edge; (a-d):[3], (e):[4] with permission of NASA;

2. Turbulence

It is a fact that most flows are turbulent, which has caught the interest of observers during history. Figure 9 is a revision of hand drawing of a free water jet issuing from a square hole into a pool, which was found in Leonardo Da Vinci's sketchbook along with a remarkable description.

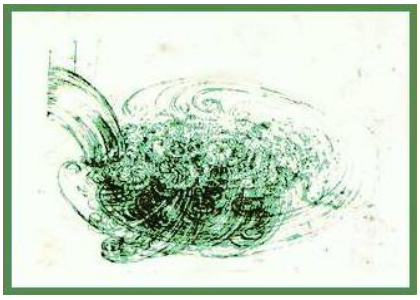

"... the smallest eddies are almost numberless, and large things are rotated only by large eddies and not by small ones, and small things are turned by small eddies and large."

Figure 9 Leonardo Da Vinci's observation of turbulent flow, with permission of eFluids.com;

Such phenomena were termed "*turbolenza*" by Da Vinci, which is the origin of the modern word for this type of fluid flows. Although turbulence has many similar characteristics to chaos, it is not exactly chaos, in the sense of the word used in analyzing dynamical systems, because turbulent flows are not only time-dependent but also space-dependent. The understanding of turbulence is one of the most fascinating, challenging and disappointing problems in classical physics. Nobelist Richard Feynman described turbulence as "the most important unsolved problem of classical physics."

Turbulent flow is featured by apparently random and chaotic three-dimensional vorticity. If there is no three-dimensional vorticity, there will be no real turbulence. The ability of generating new vorticity is essential for turbulence to maintain itself, and only in a three-dimensional mechanism the necessary turning and stretching of vortices by the flow itself is possible. The turbulence of flow results in enhanced energy dissipation and diffusivity that is responsible for the enhanced mixing and increased rates of mass, momentum and energy transports in a flow. In addition, it includes spatial and temporal intermittency, coherent structures, and high sensitivity of the instantaneous motions to the initial and boundary conditions.

There had been no considerable progress in understanding turbulent flow until the late 19th Century, beginning with Boussinesq in the year 1877 and Reynolds in 1883. Boussinesq hypothesized that turbulent stresses are linearly proportional to mean strain rates, "eddy viscosities" which is still the keystone of most turbulence models. Reynolds was the first who investigates the transition from laminar to turbulent flow by injecting a dye streak into the flow through a pipe having smooth

transparent walls, Figure 10. His observations led to identification of a single dimensionless parameter, now called the Reynolds number (Re), which characterizes flow behavior in this situation. Figure 11 provides an outline that the century between Reynolds' experiments in 1883 to the present time is divided into three overlapping period, statistical, structural and deterministic movement [5].

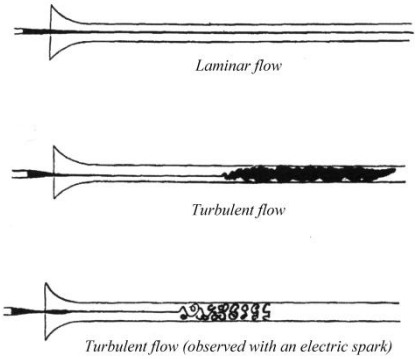

Figure 10 Reynolds' observations in his experiments [Image source: Wikimedia];

Turbulence is still a subject under studying. None actually knows a lot for sure about turbulence, and even worse, scientists even disagree about what they think they know. However, it is believed that because of chaotic-like and apparently random behavior of turbulence, determining the instantaneous motions of fluid is too complicated, and instead, we should rely on statistical methods for most of the studies.

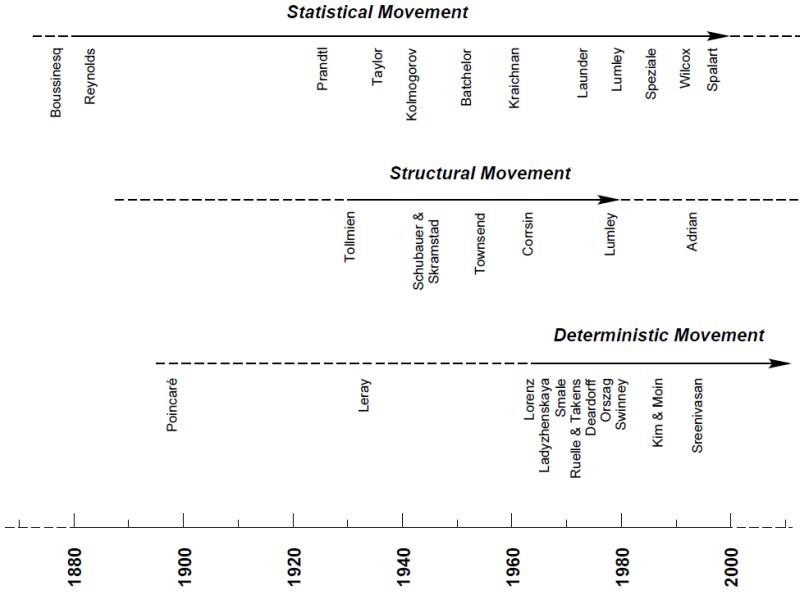

Figure 11 Movements in the study of turbulence, as described by Prof. J. M. McDonough [5];

2.1. Wall-bounded turbulent flow

Wall-bounded turbulent flows are inhomogeneous flows in the wall normal direction with a mean velocity gradient in the presence of boundaries. The solid surfaces are the responsible of necessary vorticity generation for turbulence in the absence of any other sources. These vorticities dominate the wall layer dynamics.

The vorticities are generated at the wall, where an oncoming flow is brought to rest to satisfy the no-slip condition. Then they are diffused, transported and amplified, in a turbulence regeneration cycle. The presence of the wall causes that the three-dimensional vortices, vital for the turbulence, develop more slowly than boundary free shear flow because solid walls suppress the growth of velocity components normal to the wall, and then reduce the entrainment rate.

Once the vorticity is produced, the vortex filament oriented spanwise to the mean flow lifts. The part of the filament lying further away from the wall, head, experiences higher mean flow velocity and be convected downstream faster than its parts lying lower, legs. Therefore, the filament would be stretched and intensified. The hairpin shaped vortices are formed above the viscous wall layer. Maintained upon evolution, these vortical structures burst and become quasi-streamwise vortices. These quasi-stream wise vortices are parallel counter-rotating vortices travelling with the mean convection velocity of the flow. The clockwise and counterclockwise, quasi-streamwise vortices produce ejections on the upwash side and sweeps on the downwash side. These vortices lay and bound the low-speed streaks as arranged in a series of alternating intervals. The low-speed streaks are lifted by the ejection events.

The clockwise and counterclockwise quasi-streamwise vortices are rarely paired in equal size and strength. In most of cases, each mature quasi-stream wise vortex follows a small quasi-stream wise vortex of opposite sign, offspring vortex, interpreted as the rear, wall-touching end of a counter-rotating quasi-streamwise vortex farther downstream. However, on occasion, there are also pairs of quasi-streamwise vortices with equal strength, characterizing the legs of the so-called horseshoe vortices. A sketch of the coherent structures of wall turbulence is depicted in Figure 12. For more detail, the reader is referred to references [6-10]

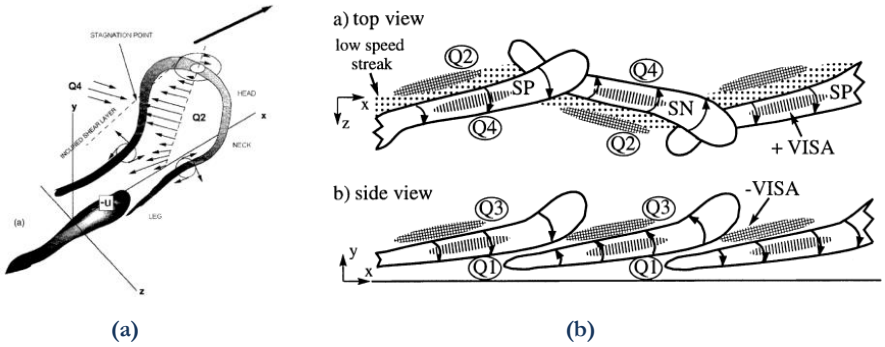

Figure 12 (a) Schematic of a hairpin shaped vortex; **(b)** Near-wall coherent structures and associated coherent events; quadrant Re stresses: Q1 and Q2 (ejection), Q3 and Q4 (sweep); (a): [10], (b): [7], courtesy of Prof. R.J. Adrian;

3. Dispersed multiphase flow

Measuring, simulating and understanding turbulent dispersed multiphase flows with particles suspended are both fundamentally interesting in science and important in industry. The presence of particle in turbulent flows has three main research aspects: 1) the preferential concentration and the dynamics of particles, 2) the effect of turbulence on the coupling between the dispersed and carrier phases, 3) the modulation of carrier phase turbulence due to the presence of particles. In addition, when the particle is not spherical, the orientation of particle in the flow is significant.

The phenomenon of preferential accumulation has been studied for years by Maxey [11, 12], Elghobashi & Truesdell [13], Eaton & Fessler [14], and others. It is well known that even in isotropic turbulence, particle distribution is not uniform. In practice, solid particles have a tendency to accumulate close to a solid surface. Wang & Maxey inferred that preferential concentration is controlled by vortical structures of small-scale turbulence. Numerical and experimental results have shown this to be correct, although it is not tested at high Reynolds numbers.

The effect of turbulence of flow on the mass, momentum, and energy coupling between the phases is significant and the key elements in physics of fluid. In momentum coupling, in the limit of zero particle Reynolds number, steady and unsteady Stokes flow approximation have been used to obtain analytic expressions for the quasi steady, pressure gradient, added mass, and Basset history components of the force. In finite Re or for non-spherical particles, empirical corrections are in common use and are strictly applicable. The results of experimental measurements of the inter-phase force on a particle have not been conclusive. In addition, the contribution of very small scale eddies to be best accounted in terms of a stochastic

component in force formulation is an area for future research. The above discussion on momentum is applicable to mass and the inter-phase exchange of energy [15].

Turbulence modulation by particles is another noteworthy aspect of particle-laden turbulent flow research. However, the turbulence modification mechanism is not properly understood due to the wide range of relevant scales and difficulties of measuring turbulence with the presence of particles. For instance, previous studies had shown that a dilute dispersion of fine particles could either augment or attenuate the gas-phase turbulent kinetic energy (TKE) although numerical simulation models do not accurately capture such turbulence modulation because the models do not include flow distortion in the order of the particle diameter or the small scales of flow [16]. It has been observed that the cases with particle sizes smaller than the Kolmogorov length scale of carrier phase turbulence had turbulence attenuation and considerable turbulence augmentation for particles larger than the Kolmogorov length scale. The measurements done by Tanaka & Eaton [16] also revealed strong damping of the turbulent kinetic energy and strong augmentation of the dissipation rate in a region surrounding the spherical particles.

3.1. Rod-like particle laden turbulent flow

As already mentioned, in many conditions the particles are non-spherical. The vast majority of numerical studies has assumed ellipsoidal particles as a simple model of non-spheres. Plenty of laboratory works has considered rod-like particles or fibers as a representative of non-spherical particles, which the length to diameter ratio plays the same role as the aspect ratio for ellipsoids. In addition, the fibers can be treated as elongated ellipsoidal particles widely used in computational works, which move according to their inertia and hydrodynamic drag and rotate under hydrodynamic torques. The main feature of anisotropic nature of the non-spherical particles is the coupling between the translational and rotational moment due to the particle orientation.

Some first investigations have concentrated on the deposition and orientation of fibers or ellipsoidal particles in a turbulent flow. Shapiro and Goldenberg[17] developed an experimental technique to measure the deposition velocity of glass fibers in a turbulent pipe flow. They found that the shape of particle significantly affects the deposition velocity of non-spherical particles, characterized by intermediate values of the effective relaxation time. They proposed semi-empirical correlations for turbulent deposition velocities of non-spherical particles.

Fan and Ahmadi[18] presented a sublayer model for the deposition of ellipsoidal particles in a wall-bounded turbulence. They showed that the trajectories for

ellipsoidal particles are sensitive functions of particle initial orientation. They also studied the effects of particle size, aspect ratio, density and gravity direction on the deposition rate of ellipsoids.

Newsom and Bruce[19] experimentally and numerically studied the orientational characteristics of relatively large fibrous aerosols in the atmospheric turbulent boundary layer. Their experiments showed that fibers with larger diameters tend to exhibit a greater tendency for horizontal orientation. The orientational preference is more sensitive to fiber diameter than to length. However, the proposed model overestimated the observed mean orientation. Olson [20] described the state of fibers suspended in a turbulent flow in terms of Probability Density Function (PDF) of fiber orientation and deposition through a stochastic model of homogeneous and isotropic turbulence.

Zhang et al. [21] studied the transport and deposition of ellipsoidal particles in a turbulent channel flow by the direct numerical simulation (DNS). While the Eulerian approach had been accepted for the turbulence field, the particles were treated in a Lagrangian approach. The prolate ellipsoidal particles reproduce quite reasonably the behavior of rigid elongated fibers. They provided the great results: *i)* The eddy structures of the near-wall turbulent flows have a key role for the particle transport and deposition; *ii)* Both spherical and ellipsoidal particles tend to accumulate in the viscous sublayer, and moreover ellipsoidal particles tend to accumulate in certain streaks due to the wall coherent vortical structures of turbulence; *iii)* The dispersion and transport of particles with large response times are mostly governed by the turbulent flow, and the particle aspect ratio has a small contribution. However, the aspect ratio plays a prominent role in the deposition rate; *iv)* Ellipsoids mostly rotate about the axis in spanwise direction due to streamwise mean shear field with little rotation about the other axes; *v)* Ellipsoidal particles tend to be aligned in the mean flow direction; *vi)* In general, the spherical and ellipsoidal particles move faster than the surrounding fluid in the streamwise direction;

Moses et al. [22] performed an experimental investigation of fiber motion near the wall in shear flow. They showed that the fiber experiences an increased rate of rotation in comparison with Jeffery's prediction for distances less than a fiber length and larger than fiber diameter from the wall. In this region, the wall effect is higher for longer fibers and is also a function of fiber orientation. The fibers oriented normal to the wall rotated faster than those that are parallel with the wall at the same distance. Once the fiber becomes aligned with the wall, its rotation gets stopped. Thus, the wall has a stabilizing effect in this orientation. In addition, their

results showed that the fibers having higher aspect ratio rotate more quickly near the wall than those with lower aspect ratio.

Paschkewitz et al. [23] presented the results of a direct numerical simulation of the drag reduction induced by rigid fibers in turbulent channel Flow. Flow statistics showed that Reynolds stresses are reduced; the fluctuations of wall-normal velocity and spanwise velocity are reduced while streamwise fluctuations are increased, and streamwise vorticity is reduced. Melander and Rasmuson[24] simultaneously measured the concentration and velocity of wood fibers suspended in the air by the method developed on PIV technique using fibers as seeding particles. This made their velocity measurements less accurate and reliable.

Xu and Aidun [25] measured the effect of fiber concentration and Reynolds number on the shape of the velocity profile of fiber suspension flow in a rectangular channel by Pulsed Ultrasonic Doppler Velocimetry (PUDV). They found that the presence of fiber in the suspension decreases the turbulence intensity and hence reduces the turbulent momentum transfer. On the other hand, fibers in the suspension tend to flocculation, which will grow the momentum transfer. The relative contribution of these two types of momentum flux will determine the final shape of the velocity profile.

Shin and Koch[26] presented results of a parametric study in a direct simulation of the translational and rotational motion of slender fibers in isotropic turbulence in order to realize how the translational and rotational dispersion of fibers depends on fiber length and the Reynolds number of the turbulent flow. The fibers having lengths smaller than the Kolmogorov length scale move like fluid particles and rotate like material lines. With increasing fiber length, the fiber becomes insensitive to the smaller-scale eddies so that the translational and rotational motions of fiber is slower.

The influence of homogeneous isotropic grid-generated turbulence on the orientation distribution of a dilute suspension of stiff fibers in a planar contraction is experimentally studied by Parsheh et al. [27]. They utilized high-speed imaging and Laser Doppler Anemometry (LDA) techniques to quantify fiber orientation distribution and turbulence characteristics. Their results showed that the characteristics of inlet turbulence have a high influence on rotational diffusion. Moreover, the flow Reynolds number has negligible effect on the development of orientation anisotropy, and the influence of turbulence on fiber rotation is insignificant for rotary Peclet number larger than 10. Using PIV measurements of the structures of sedimentation flow, Metzger et al.[28] investigated the instability of a sediment suspension of rigid and high aspect ratio fibers within a viscous fluid. Their observations confirmed the existence of instability. They reported the mean

velocities and velocity fluctuations; the strength of the velocity fluctuations strongly correlates with the size of the vertical component of the sedimentation structure.

Mortensen et al.[29] studied the dynamical behavior of small elongated ellipsoidal particles in channel turbulent flow by means of DNS and Lagrangian particle tracking. Their approach was similar to which taken by Zhang et al. but their focus was on the effect of particle aspect ratio and the particle stokes number on the distribution, orientation, translation, and rotation of particle. They found that the aspect ratio practically does not have any influence on the translational motion, whereas both mean and fluctuating spin components depend crucially on it. The prolate particles have a tendency to align themselves with the mean flow direction. In addition, ellipsoidal particles like spherical particles tend to accumulate in the viscous sublayer and preferentially concentrate in regions of low speed fluid velocity. The orientation, distribution, and deposition of fibers in a directly simulated turbulent channel flow is investigated by Marchioli et al. [30], as well. Their results confirmed that fibers tend to be oriented in the mean streamwise flow direction near wall. However, for higher fiber inertia this alignment with streamwise direction is just stable for rather short times before fibers rotate in the vertical plane. The orientational and translational behaviors of fiber affect the process of fiber accumulation at the wall. Comparing the behavior of fibers with that of spherical particles demonstrated that the aspect ratio has little influence on clustering, preferential distribution, and segregation. They observed no preferential orientation and no significant segregation in the channel centerline, which confirms that the role of inertia and elongated shape becomes less prominent in far region from wall. Andersson et al.[31] developed a novel scheme for strong coupling between inertial Lagrangian point particles and a continuous Eulerian fluid phase, and presented a two-way coupled simulations of prolate particle laden turbulent channel flow. M. Do-Quang et al. [32] simulated almost neutrally buoyant finite-size rigid fibers in turbulent channel flow through DNS. They showed that the finite size leads to fiber-turbulence interactions that are significantly different from earlier numerical studies for elongated ellipsoids smaller than the Kolmogorov scale. Their simulations indicated that the finite-size fibers tend to stay in the high-speed streaks due to collisions with the wall. In the central region of the channel, long fibers tend to align in the spanwise direction while very close to the wall they become mostly aligned in the streamwise direction.

G. Bellani et al. [33] experimentally investigated shape effects on turbulence modulation. They found that ellipsoidal particles cause less reduction of the mean Turbulent Kinetic Energy (TKE) in comparison with spherical particles. The reason for this is changes in production and dissipation of TKE, as well as redistribution of TKE across scales by ellipsoids and spheres. R. Van Hout et al.

[34] proposed a combined PIV and digital holographic cinematography to study the fiber-flow interaction mechanisms in turbulent flow. They focused on the extraction of the velocity field in the vicinity of the fibers and their rotational and translation motion. When they applied in-line digital holography to image the fiber orientation and positions, the fiber diameters were not resolved in a high resolution, but their lengths were different. Their PIV results showed a relation between the instantaneous vorticity field and the fiber orientation. However, they explained that a larger ensemble size is needed to confirm this in a statistical sense.

Chapter 2

Particle Image Velocimetry and Particle Tracking Velocimetry

There are two fundamental approaches to understanding fluid flows experimentally, *Visualization* and *Measurement*. Visual inspection has probably always played a pivotal role in the understanding of complex phenomena, since "seeing is believing". Visualization is accomplished by adding visual markers to the originally invisible flows. Common techniques are the injection of dye, marker particles or hydrogen bubbles into liquid/water. Airflow can be made visible by means of, for example, smoke or tufts attached to a surface. Photographs can be used to document the findings. When dynamic, time-dependent phenomena should be presented, specialized filming techniques related to the time scale of the flow are required. On the other hand, measurements provide quantitative information of a flow. Generally, the flow velocity can be acquired at one single position in space, point-based measurement, by pitot tubes, hot-wires probes or anemometers. In this type of measuring fluid velocity, the probe may spoil the flow around it inevitably due to the mechanical measurement principle.

Particle Image Velocimetry (PIV) and Particle Tracking Velocimetry (PTV) can be regarded as the development of flow visualization techniques, which offer the solution to combine the methods of visualization and measurement into one process. They are *optical*, *entire field*, *non-intrusive*, and *indirect* techniques providing an accurate quantitative measure of the instantaneous flow velocity field across a region of the flow field, wherever optical access is achievable. "Entire-field" means that the flow velocity field can be measured simultaneously over a defined area (Field of View), in contrast to single point-based measurement. "Non-intrusive" is the absence of any probe parts that might disturb the flow within the measurement area. PIV and PTV extract the fluid velocity from the tracer particles motion, thus we measure the velocity of flow indirectly.

The basic principle for the velocity field measurement is described as the flow seeded using tracer particles is recorded sequentially by image acquisition devices in the time interval Δt, and images are processed to extract the particle displacement

Δs using image processing techniques during the time interval Δt. The velocity is estimated by the fundamental definition:

$$V = lim_{\Delta t \to 0} \left(\frac{\Delta s}{\Delta t} \right)$$

However, the experimental problem is that it cannot be taken in the limit as Δt tends to zero. The time step Δt is chosen such as to accurately determining the displacement Δs.

PIV image processing technique primarily depends on the available equipment to record the particle image and the seeding particle concentration. There are three types of fundamental algorithms for processing: auto-correlation, cross-correlation and particle tracking. The correlation-based processing techniques estimate spatially averaged velocities on small cells, known as PIV. In PIV, The flow seeded in the field of view is resolved by a grid of typically about 100-150 discrete small cells (interrogation windows) yielding velocity vectors. The interrogation window size determines the grid size of the vector field; it is comparable to computational mesh in computational fluid dynamics (CFD). Dynamical conditions can be resolved at high sampling rate in the KHz range; alternatively steady conditions can be observed at sampling rates below 1 Hz. These spatial and temporal resolutions allow detailed analyses of the physics of flow by means of statistics and velocity field visualization. These advantages are the reason why PIV is often applied when it comes to comparison between experimental and numerical results. In PTV, the individual particles embedded in the flow are tracked to identify the displacement of particles. It is often defined as the low particle density variant of PIV.

PIV and PTV are techniques that involve many scientific disciplines including advanced optics, laser physics, signal and image processing, data handling and especially health and safety regulations. Therefore, background knowledge in these disciplines will be helpful to overcome the specific challenges that come up in the daily PIV usage.

1. Principle of PIV operation

The PIV working principle is quite simple. The flow is seeded with tiny, neutrally buoyant, light reflecting particles as tracer. Using a light sheet, formed by passing a double pulsed laser beam through an optical arrangement including cylindrical lenses, the particles in the measurement plane of the flow are illuminated twice with a small time interval. Camera is used to record two exposures of the light scattered by the tracer particles. Depending on the flow velocity and the magnification factor of the camera lens the delay of the two pulses has to be chosen such that adequate displacements of the particle images are obtained on the imaging

sensor of the camera. In general, only two components of instantaneous velocity can be measured using standard PIV (2D PIV). All the three-velocity components measurement is done by a stereoscopic approach (Stereo PIV). The favored arrangement of a 2D PIV system is that the biggest velocity component of the observed flow field is parallel to the light sheet while the viewing direction of camera is normal to the light sheet, as shown in Figure 13. Even when the arrangement is restricted for optical access by experimental boundary conditions, the setup should not differ too much from the ideal perpendicular arrangement in order to keep systematic errors as small as possible.

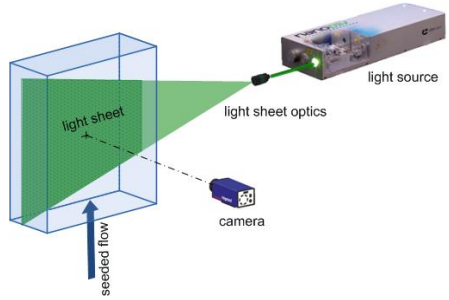

Figure 13 A 2D PIV system;

The two exposures should be taken within a short time interval so that the same particles are caught in both exposures. The two exposures may be recorded on either a single image (double exposure-single frame) or two consecutive images (double exposure-double frame). Evaluating image in the first method is based on autocorrelation. This results in a directional vagueness. Therefore, when this method is used, the flow must only be in one direction. The double exposure-double frame method along with cross-correlation processing method is more commonly used, and here it has been also applied. The remaining part of this chapter will deal with this method.

In the evaluation of the PIV images, it is assumed that the tracers follow the local flow between the two illuminations. The image frames are divided into a large number of small interrogation windows. Each interrogation window should include at least ten tracer particles on average. A local displacement vector is estimated within each interrogation window using cross-correlation processing. The velocity is calculated using the time between the image shots and the physical size of each pixel on the camera. A schematic example of procedure of PIV recording and analyzing is shown in Figure 14.

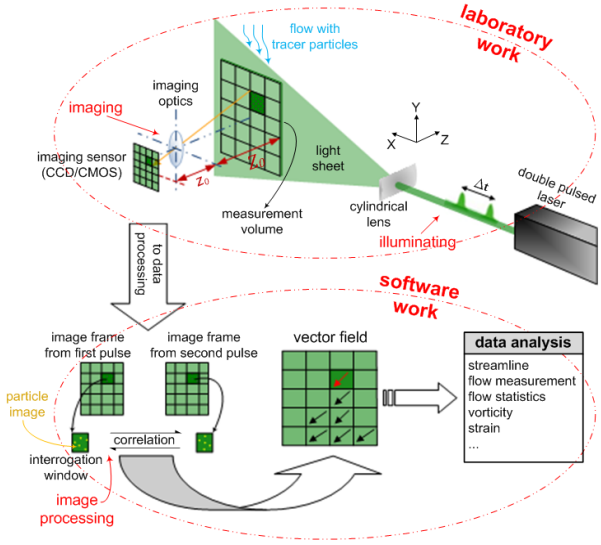

Figure 14 Common PIV procedure from laboratory works to data analysis by software;

2. PIV hardware components

2.1. Seeding

Actually in PIV measurements, the particle movement is recorded; not the flow is measured directly. Therefore, it is necessary that the flow is seeded with particles scattering the light in order to image the flow field. The particles should be ideally spherical, and small enough to follow the flow, but large enough to scatter the required amount of light. The choice of size also depends on the flow scales that shall be resolved. Indeed, the particle Stokes number (particle response time) must be less than 0.1 to follow fluid streamlines closely with tracing accuracy below 1%. In water, the most commonly used particles are polyamide powder (PSP) and hollow glass spheres that are sometimes coated by silver (SHG) to enhance reflectivity. Usually, smoke is used in airflow measurements in a wind tunnel. We must make sure that the seeding is distributed uniformly in the flow.

2.2. Light source

Commonly a Q-switched pulsed Nd:YAG laser (Neodymium Yttrium Aluminum Garnet) or Nd:YLF laser (Neodymium-doped Yttrium Lithium Fluoride) is used as the light source because of their high and stable light intensity. Pulsed lasers need some time to build up energy before they can fire a new pulse while the PIV image pair needs to be taken within a quite short period. Therefore, a laser system with double cavities is usually used. The laser pulses have a duration of 5-200 ns and energy in each pulse can be up to 500 mJ. However, the light energy decreases with the increase of repetition rate, Figure 15. Shuttered Continuous

Wave (CW) lasers that provide a compact and cost-effective light source are also used in low-speed PIV imaging applications.

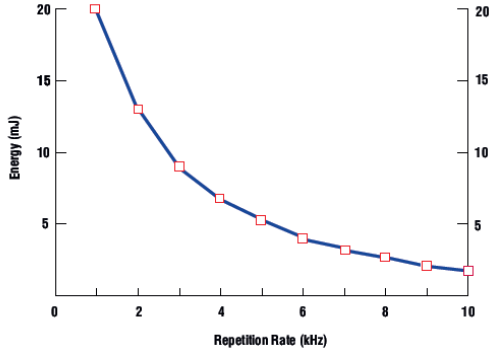

Figure 15 Light energy versus repetition rate for Litron LDY-300, with permission of Litron Laser ltd;

The lasers of Nd:YAG and Nd:YLF emit monochrome light with a wavelength of 1064 nm, which is in the infrared range. For PIV purposes, light with this wavelength is not useful since the most of cameras have their maximum sensitivity in the blue-green part of the spectrum. Another disadvantage is the light sheet is not visible when positioning it in the measurement area. For these reasons, the wavelength of these lasers is halved by harmonic generator and IR light-dump, so it becomes 532 nm. Figure 16 depicts the basic layout of a common PIV-laser. The beam coming out from the laser source has a quasi-circular cross section that has to be shaped through a cylindrical lens in order to form a planar light sheet.

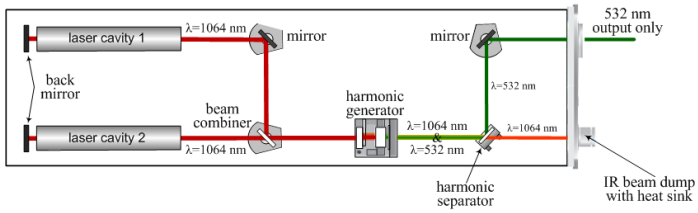

Figure 16 Dual cavity laser for PIV;

In general, for applications in gas flows, a high power light source for illumination of the tiny tracer particles (or smoke) is required in order to charge the imaging sensor well. In liquid flows, larger particles that scatter much more light can usually be accepted. Therefore, light sources of considerably lower power can be utilized here. In most applications, a compromise must be found.

PIV laser beams are extremely harmful to the body. It needs to be handled with care, and relevant health and safety rules must be followed.

2.3. Camera

When the PIV technique was young and immature (in the late 1960's), the recording medium for PIV images was photographic films. The records were analyzed by a laser interference method and applying an optical Fourier transform. It resulted in a time-consuming data extraction. Later, the photographs were scanned after exposure and digital signal processing methods were employed for analyzing. The fast progress of PIV came with the availability of digital cameras and the development of numerical analysis methods. Digital PIV cameras are typically characterized by their maximum recording rates (kHz) and their maximum resolution (MPx). However, there is still the problem of combination of frame rate, resolution and sensitivity. When higher recording rates are desired, the resolution must be reduced in the interest of high frame rates, Figure 17. It is due to limitation on technology of pixels charge transferring to the image buffer. Photographic film may still be a viable choice when high resolutions are required.

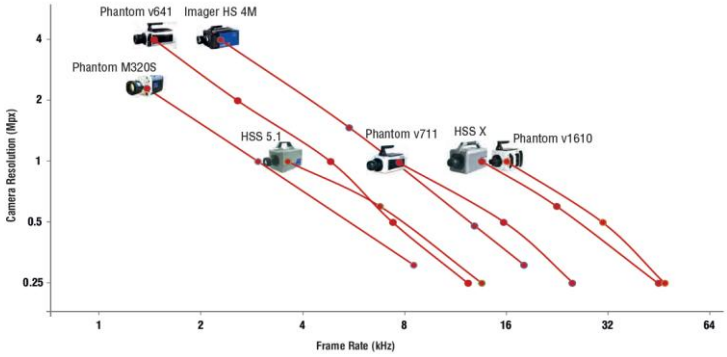

Figure 17 The working range of a few popular time-resolved PIV cameras, with permission of LaVision GmbH;

The imaging sensor of the digital PIV cameras can be either Charged Coupled Device (CCD) or Complementary Metal Oxide Semiconductor (CMOS). CCD and CMOS sensor technology have evolved rapidly in recent years to provide both high pixel count and high frame rates with high sensitivity and low background noise. CCD camera is the classic technology recording consecutive frames, which are generally cheaper but comparably slower in acquisition rate (max 20 Hz). CMOS cameras can reach very high frame rate (10 KHz), suitable for high-speed imaging, but yet more expensive. CMOS cameras do not record sequential frames as such, instead a spaced series of image pair on chip. The architecture difference between CMOS and CCD sensor imply the demand of an entirely different synchronization.

Nowadays, with the advent of high frame-rate digital cameras and pulse light sources with high repetition rate, it is possible to obtain instantaneous vector maps of the flow field with high spatial resolution, which are time-revolved.

2.4. Synchronization unit

Synchronizing of light pulse timing with the camera and controlling of the light pulse duration and the interval between pulses is necessary. A programmable synchronization unit triggers the laser pulse and the camera in a specific sequence to allow images to be acquired. The duration of the light pulse must be large so that the light scattered from particle can charge the chip. On the other hand, it must be short enough to freeze the motion of the particles during the pulse exposure in order to avoid blurred particle image. The time delay between the illumination pulses must be long enough to be able to determine the particle displacement between the images with sufficient resolution and short enough to avoid out-of-plane losses of the particles leaving the light sheet between successive illuminations. Short inter-exposure times can be achieved by two different mode.

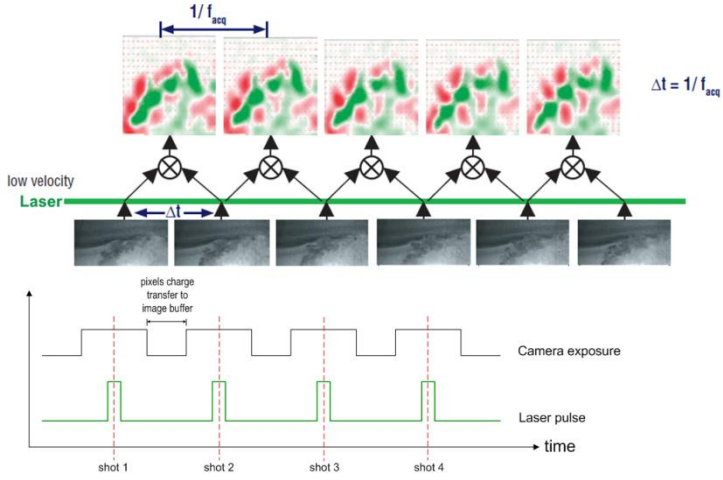

Figure 18 A schematic timing overview for time series mode;

In the mode of time series measurement, a single laser pulse is triggered for each camera shot. From each pair of neighbor images, a vector field is computed so that the camera frame rate is equal to the acquisition frequency, Figure 18. The acquisition rate should be selected such that the resulting time between laser pulses ($\Delta t = 1/f_{acq}$) is adequate for the flow velocities within the field of view. This mode provides time-resolved vector fields. These data can yield time-related information such as power spectra, Lagrangian tracking and space-time correlations.

For too high flow velocities to be captured by time interval equal to acquisition rate, pairs of images can be taken by letting the first laser pulse be fired at the end of the exposure of the first frame and the second pulse at the beginning of the exposure of the second frame. This mode gives the user flexibility in choosing a

time interval with no coupling with the camera frame rate. With this mode, velocity fields are less correlated in time than with previous mode mentioned.

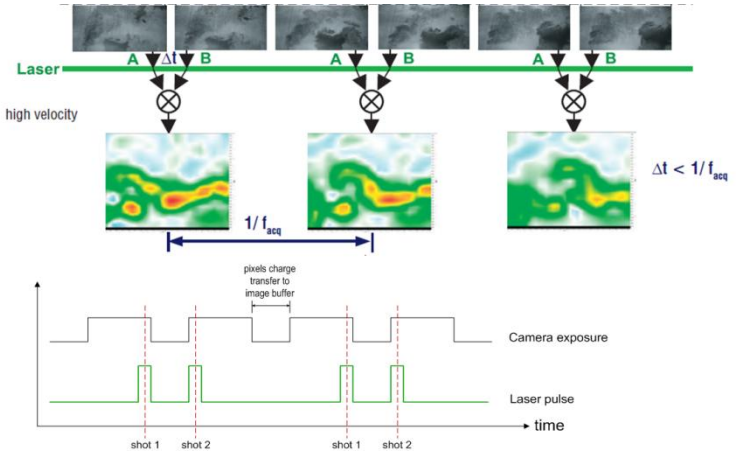

Figure 19 A schematic timing overview for very high velocity measurement;

3. PIV adjustment

3.1. Light Sheet Adjustment

The beam emitted by the light source is shaped into a thin sheet via cylindrical and spherical lenses. Common arrangement is illustrated in Figure 20. The sheet width (D) at a distance L is a function of focal length of the cylindrical lens f_1. In this arrangement, illumination is not uniform along the propagation direction. Other arrangements should be applied when uniform illumination is strictly required.

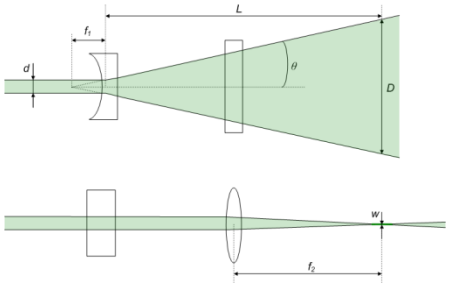

Figure 20 Light sheet formation optics;

$D = 2L\tan\theta + d$ light sheet width

$\theta = \arctan\left(\frac{d/2}{f_1}\right)$ divergence angle

$w = 2\frac{2.44\,\lambda\,f_2}{d}$ sheet waist thickness

A desired width of the light sheet is needed to minimize loss of the light. It depends on the size of the measurement region and the distance between the sheet optics and the measurement region. The laser light must be focused in the region so that the minimum thickness (waist) of light sheet is placed within the measurement

area, Figure 21. The reason to use the narrow dent of the laser sheet is to minimize the equivalent measurement volume that has to be considered in PIV measurements.

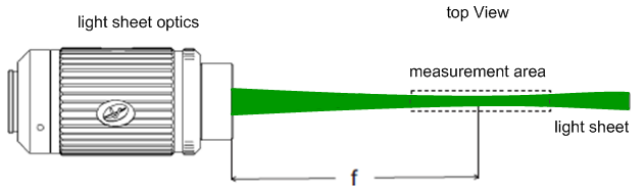

Figure 21 Light sheet focusing;

3.2. Optical adjustment

From a practical viewpoint, the particles must be visible in the images as sharp and clear as possible. In addition, optical considerations are needed for an accurate PIV measurement, such as estimating the dynamic range of the measurement system.

-Scattering properties of tracer particles

As explained previously, to fulfil the fluid mechanical requirements demands small particles as tracer. However, the tracers should scatter enough light to be visible. Typical particle size is on the order of a micrometer for gas flows, and tens of micrometers for liquid flows, where the particle diameter d_p is larger than the light wavelength (typically λ=532 nm). This means that the light scattering pattern from particle is *Mie* scattering. A *Mie* scattering diagram is shown in Figure 22. Most of the light is scattered in the forward and backward direction. At a scattering angle of 90°, the scattering amplitude is low. This is why a PIV camera with the optical axis normal to the light sheet needs generally a strong light source.

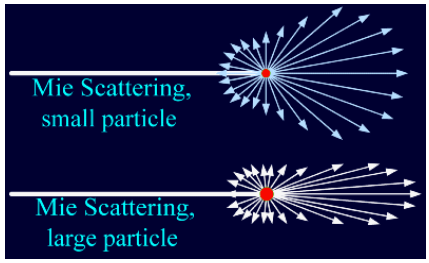

Figure 22 Scattered light intensity as a function of the scattering angle for two different particle sizes;

The particle scattering cross section (accordingly scattered light intensity) is roughly proportional to the d_p^2 and also depends on the particle material refractive index relative to the refractive index of the surrounding medium and the light

wavelength. Another approach is to use fluorescent-dye covered particles, in which way the light is absorbed by the dye and is then re-emitted at another wavelength.

-Imaging and optical configuration

Figure 23 illustrates the PIV optical configuration for image acquisition. The image of illuminated particles within the laser sheet with the thickness of ΔZ_0 are formed by means of an imaging lens on the recording medium (CCD or CMOS) in the image plane. The lens is characterized by its focal length f and aperture number $f\#$ (the ratio of focal length and aperture diameter). From the geometrical lens law, we have:

$$\frac{1}{Z_0} + \frac{1}{z_0} = \frac{1}{f}$$

Where z_0 is the image distance to the lens, and Z_0 is the object distance to lens. The image magnification factor is defined as:

$$M_0 = z_0/Z_0$$

The recorded image diameter d_τ of a small particle with real diameter d_p on the image plane is given by [35]:

$$d_\tau^2 = d_e^2 + d_r^2$$

Where d_e presents the diameter of optical image prior to being recorded, and d_r is the resolution of the recording medium (the resolution elements of a CCD or CMOS chip are the pixel elements, and the resolution d_r is characterized by their spacing). The diameter of the diffracted image of the particle is:

$$d_e^2 = d_s^2 + M_0^2.d_p^2 \ , \quad with:\ d_s = 2.44(1 + M_0)f\#\lambda$$

Where d_s is the diffraction-limited spot diameter, and $M_0.d_p$ presents the geometric image diameter. For typical optical arrangement in PIV, it is found that $d_s >> M_0 d_p$, so that $d_e \approx d_s$. In other word, the diffraction effect is generally dominant, and the particle image diameter is quite uniform despite variations in d_p.

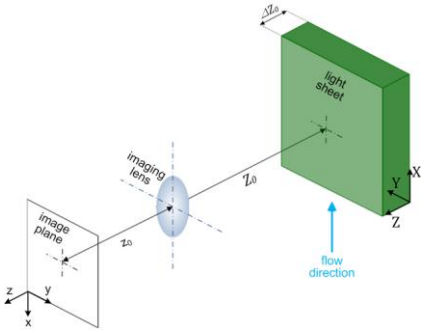

Figure 23 Schematic illustration of the optical configuration for PIV imaging;

All illuminated particles should be in focus. This condition is fulfilled if the thickness of the light sheet is equal to or smaller than the depth of field (DoF) in the imaging arrangement. The depth-of-field of the image (δz), the range of distances in object space for which object is imaged with acceptable sharpness with a fixed position of the image plane, is given by the following equation. The depth-of-field is frequently a constraint imposed on the PIV measurement arrangement.

$$\delta z = 4(1 + 1/M_0)^2 f\#^2 \lambda$$

These equations dedicate the lower limit for the particle image diameter and are applied for an aberration free lens with a circular aperture.

3.3. Seeding concentration

The mathematical analysis utilized to estimate the particle displacement strictly depends on the seeding concentration. For low seeding density cases, the particles can be individually tracked, this approach known as PTV (explained in details in section 9). In measurements where the inter-particle distance specifies the upper limit for the spatial resolution, a high seeding density is desired, and a PIV statistical evaluation is required to determine the particle displacement, Figure 24.

The seeding concentration has primary effects on the evaluation of PIV recordings. In general, It influences the particle image density and thus the measurement uncertainty substantially. The number of particle pairs in two successive images depends on the overall seeding concentration and interrogation window size. A higher number of particle image pairs increase the signal to noise strength in the correlation analysis, thus it increases the probability of valid displacement detection. Moreover, higher seeding density allows the use of smaller interrogation windows which ensures a high spatial resolution. However, the increase in the seeding concentration reduces the optical transparency of the flow. Monte Carlo simulations for double frame-double exposure PIV recordings have showed that for $N_I F_I F_O > 5$, the valid detection probability is over 95%, where N_I is the particle image number in an interrogation window, F_I and F_O are the factors of in-plane particle pair loss and out-of-plane particle pair loss. Usually, for optimization of the seeding concentration and interrogation window size, it is sufficient to ensure the presence of at least five particle pairs within interrogation windows.

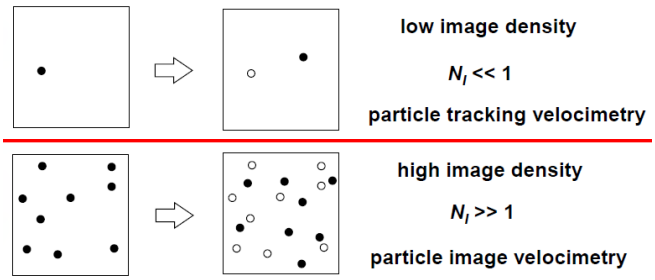

Figure 24 Strategies for low seeding density and high seeding density; filled circles: the particles at the first frame; hollow circle: the particles at the second frame;

3.4. Illumination pulse duration

The duration of the laser pulse (or the image exposure time for continuous illumination) should be short enough to give clear circular dots in the image instead of a blurred streak of the tracers. This is obtained when the particle image shift within the light exposure is considerably smaller than the particle image size (d_τ).

$$\delta t \ll \frac{d_\tau}{V}$$

On the other hand, the pulse duration should be large enough so that the light scattered from the particle can charge the imaging sensor on the camera chip.

3.5. Illumination pulses separation adjustment

In general, accurate velocity measurements require a short time interval, which in turn introduces the uncertainty associated with the particle displacement measurement. Small particle displacements reduce the dynamic velocity range and is associated with large displacement measurement error. On the other hand, large particle displacements reduce the spatial resolution.

The time delay between illumination pulses has to be adjusted in a manner that the particle image shift (Δs) is in the interval given by the resolution of the system and the maximum allowable particle displacement, explained as $0.1 pixel < \Delta s < \frac{1}{4} D_I$, where D_I is interrogation window side length. In addition, to avoid out-of-plane losses, the constraint of $|\perp z| < \frac{1}{4} \perp Z_0$ ($\perp z$ is particle displacement normal to light sheet) should be satisfied. In high shear flows in order to decrease the gradient effect, it should also be $M_0/\Delta u/\Delta t < d_\tau$. These constraints strongly limit the dynamic range of PIV. As a rule of thumb, the pulse separation that give rise to a mean particle image shift about 5 pixels would be suitable.

3.6. Camera scaling

The pixels on the camera chip must be given physical size. The physical scale of the pixel depends on imaging configuration including the size of field of view, the imaging sensor size on the camera chip and the magnification factor. For normal viewing direction with no image distortion, a linear scaling (pixel/mm) is sufficient. The camera scaling can be implemented easily by locating a ruler bar in the field of view (the object plane), specifying two known points on the ruler image and designating their separation as distance in millimeter (mm) for the pixel coordinates. Otherwise, (due to oblique viewing direction, curved windows of the test section, non-linear imaging optics etc) the images need a correction based on a spatial calibration.

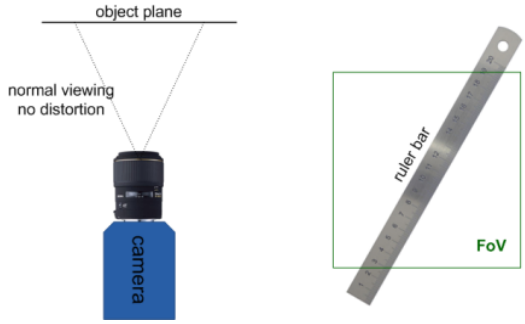

Figure 25 Camera scaling;

4. Image pre-processing

The image pre-processing will give the possibility to manage the particle image before the vector computation is performed. This often helps to enhance the quality of the results, especially if one have to work with high or locally changes in background intensities.

-Intensity inversion

The intensity Inversion can be necessary when the particle image intensity is less than the background.

-Sliding background filter

The large intensity fluctuations in the background due to reflections etc. should be subtracted from the original image. Sliding background filters out the large intensity fluctuations in the background while the small intensity fluctuations of the particle signal pass through. Therefore, one receives an image with constant background level without affecting the particle intensity. The scale length in pixel dimensions should be at least double the size of the mean image particle.

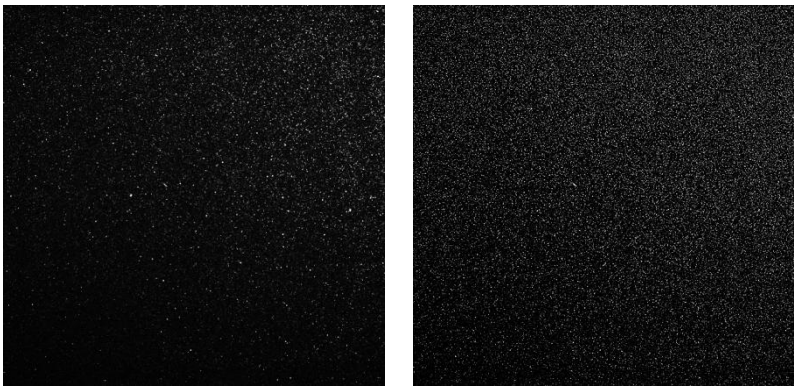

(a) original image (b) after sliding background filter

Figure 26 An example for sliding background filter;

-Particle intensity correction

The particle intensity should be corrected locally. This is especially useful if one works on particle images with a high intensity fluctuations. It can be performed using a MIN-MAX filter. The MIN-MAX filter will determine the maximum and minimum intensity on a local window specified by the filter size [in pixel]. This filter will work in the following way:

1.Takes the image and extract sliding minimum over a window in filter size.

2.Subtracts this sliding minimum from the original image. This procedure removes the local background intensity level.

3.Calculates a sliding maximum over a window in filter size.

4. Calculates sliding maximum over a window of 10×filter size to get a global maximum.

5.Divides the results of step 3 by the results of step 4. This is the ratio of local to the global maximum.

6.Multiplies the results from step 2 by the results of step 3.

As a result, we obtained homogeneous particle intensities so that small particles could also contribute to the correlation, Figure 27.

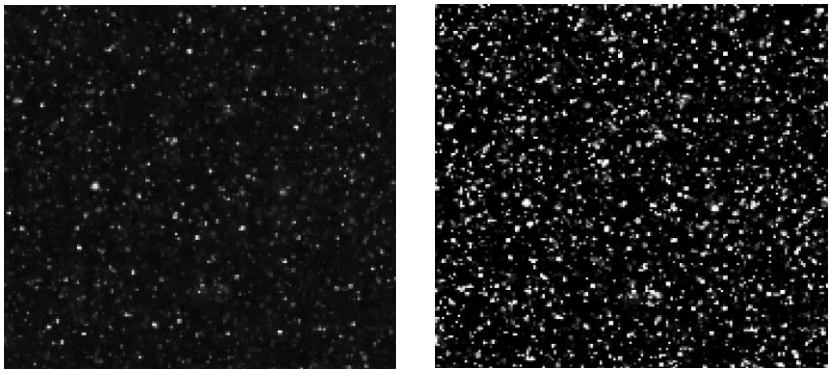

(a) original image (b) after Min-Max filter

Figure 27 Example for particle intensity correction;

5. Cross-correlation analysis

In double exposure-double frame PIV recording, the particles displacement are estimated by cross-correlation analysis. The cross-correlation function is not calculated on the whole images but on small cells called interrogation window, as already explained. The The cross-correlation can be considered as finding the most likely distance giving the best pattern match for the particles pattern that has moved within the interrogation window during the time interval. Each correlation operates only on the intensities inside the two corresponding interrogation windows. Figure 28 illustrates evaluation of PIV recordings using cross-correlation.

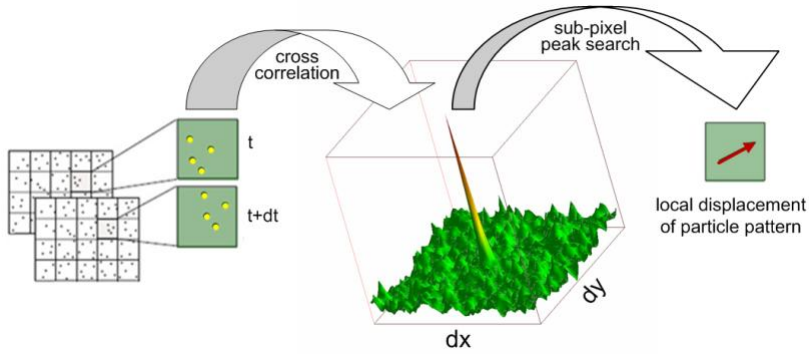

Figure 28 Cross-correlation analysis of PIV recordings;

The spatial cross-correlation function $R(\Delta s)$ is expressed by:

$$R(\Delta s) = \int_A I_1(X) I_2(X + \Delta s) dX$$

Where the interrogation windows of the first and the second images are denoted as $I_1(X)$ and $I_2(X)$, and Δs is the shift between the windows. The image intensity is separated into:

$$I = \langle I \rangle + I'$$

Mean intensity intensity fluctuation

The spatial correlation can be separated into three terms:

$$R(\Delta s) = R_c(\Delta s) + R_F(\Delta s) + R_D(\Delta s)$$

Where: R_C: mean background correlation.

R_F: correlation between mean intensity and intensity fluctuations.

R_D: correlation of image fluctuations.

The most probable displacement is determined by the position where $R(\Delta s)$ reaches its maximum value. The discrete cross-correlation approach is common in digital PIV since it can utilize the advantage of the FFT for a fast processing.

-Subpixel interpolation

After the cross-correlation calculation, a measure of the displacement is found by detecting the location of the highest correlation peak on the correlation map, but it will also introduce a bias error in evaluating the peak location. The peak detected will result in an uncertainty of ±0.5 pixel. However, the accuracy can be increased considerably by curve fitting and an interpolation scheme.

The most common way to perform the subpixel interpolation is to employ a three-point estimator. When the maximum peak has been detected at $[x_i,y_j]$ (pixel position), the neighbor values are used to fit a Gaussian function to the peak usually. Correlation peak can be approximated by a rotationally symmetrical Gaussian bell working on 3×3 or 5×5 pixel. Other ways in order to interpolate the subpixel of the peak are parabolic peak fit and peak centroid.

-Window overlap and iterative evaluation

Recent PIV methods utilize algorithms with overlapped windows and iterative evaluations with decreasing in interrogation windows size or with constant size, which can notably reduce the errors due to the image pair losses and in-plane velocity gradients simultaneously increasing the spatial resolution.

Figure 29 shows interrogation windows with 50% overlap. The interrogation window size and specified value for overlap determine the spacing of vectors in the vector field i.e. the higher the overlap percentage, the higher resolution while decrease pairs losses.

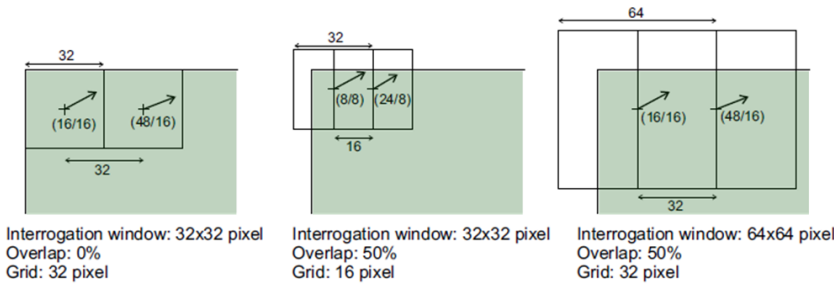

Figure 29 Vector position depending on interrogation window size and overlap;

During the iterative analysis (multi-pass), the vector field is calculated by an arbitrary number of iterations with either a decreasing interrogation window size or constant size. In general, the vector field calculated in the prior iteration will be reference vectors as the best choice for window shift in the next iteration. In this manner, the window shift is adaptively improved to ensure the same particles are correlated with each other even if one use small interrogation windows where fewer particles enter into or disappear from the interrogation window. It enhances the signal to noise ratio in correlation and the vectors in the following steps are computed more accurately and more reliably. The multi-pass with adaptive window shift and decreasing window size during the passes allows to use a much smaller final interrogation window size than it would be possible without adaptive window shifting. This improves the spatial resolution of the vector field and produces less erroneous vectors. Figure 30 illustrates the adaptive multi-pass with constant size of interrogation window.

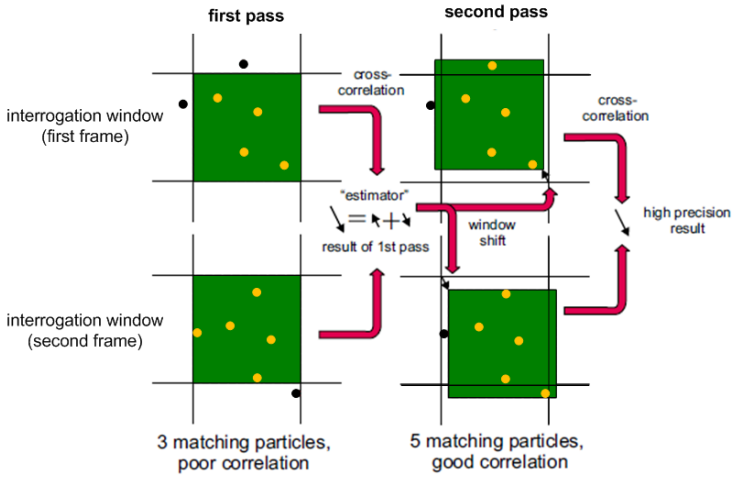

Figure 30 Adaptive multi-pass with constant interrogation;

-Window deformation

The high local gradients lead to a large particle pair loss and spoil the peak detection. The information from the initial steps can be used to stretch the interrogation window according to the shear in the flow field, Figure 31. The particle pair loss is reduced, and the signal to noise ratio is increased.

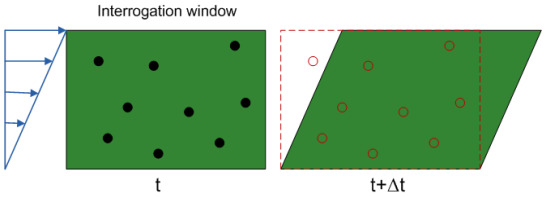

Figure 31 Deformed interrogation window;

6. Vector post-processing

Even in carefully designed PIV measurements, there is a probability that an interrogation yields a spurious vector. Although in practice the number of erroneous vectors in a PIV data set is relatively low (typically less than 5 %), their occurrence is more or less unavoidable. These vectors generally result from interrogation cells that contain insufficient particle-image pairs, and differ nonphysically in magnitude and direction from nearby valid vectors. Once a vector field has been computed, vector validation algorithms can be applied to eliminate spurious vectors.

-Allowable vector range

The Allowed vector range will restrict the filtered vectors to a specified range. The information obtained from the scatter plot, Figure 32, may be useful to select the correct range for valid vector components.

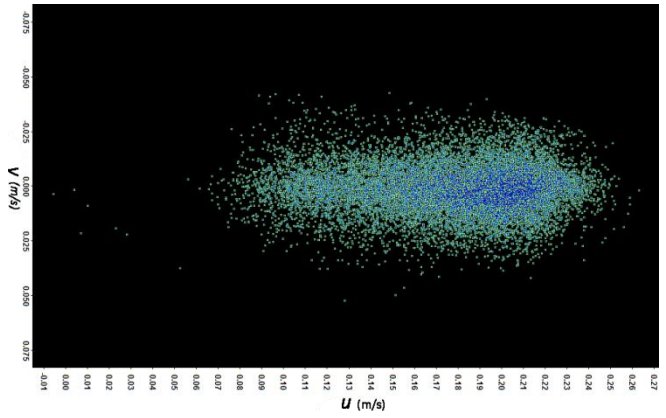

Figure 32 A sample of *u-v* scatter plot for the turbulent flow near the wall;
u: streamwise velocity, v: spanwise velocity;

-Peak Ratio

The peak ratio factor Q or the signal to noise is defined as $Q=P_1\text{-}min/P_2\text{-}min$. Where *min* is the lowest value of the correlation plane and P_1 and P_2 are the peak heights of the first and second highest correlation peak. The Q-factor can be used as a postprocessing criteria for eliminating questionable vectors below this threshold. In general, the higher Q-factor indicates more confidence in the vector. It should be noted that this procedure is quite unspecific and will also remove acceptable vectors. One would use this postprocessing procedure, when it is necessary to have as few spurious vectors as possible, e.g. when calculating flow averages and rms values. In these cases, it is better to remove all questionable vectors because erroneous vectors will spoil statistics. Accidental removal of good vectors only means that additional images are required to compute an accurate average. It should also be noted that bad vectors may also have a high peak ratio.

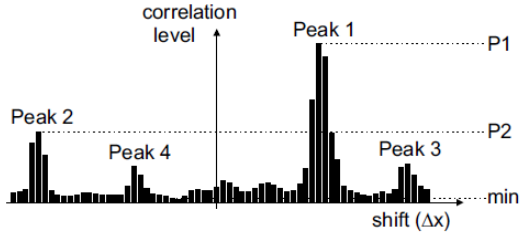

Figure 33 Peak ratio or signal to noise ratio, with permission of LaVision GmbH;

This ratio is always $Q>1$ (usually in the range of about 1.5), and if it is high (let's say above 2) it indicates that the vector is quite likely a valid vector. Peak ratios close to 1 mean that there is a high probability that the found highest peak (best vector) is a false random peak. This ratio gives a clear indication of the goodness of the vector field.

-Local Median filter

In order to find and remove erroneous vectors with more efficiency, a local median filter can be applied in post-interrogation procedure. The local median filter calculates a median vector from the neighboring vectors (usually 8 neighboring vectors) and compares the center vector with *this median vector* $\pm$ *deviation of the neighboring vectors*. Each vector component is checked independently so that the median value means that e.g. all u, v or w components are sorted independently according to their value, and the middle component is taken. The central vector is regarded as a bad vector and removed from the vector field when it is outside the allowed range.

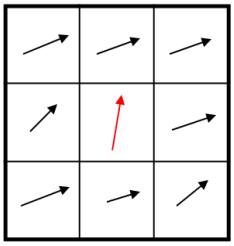

Figure 34 Local Median filter window;

Criteria for keeping a vector is:

$$Vmedian_{x,y,z} - Vrms_{x,y,z} <= Vcenter_{x,y,z} <= Vmedian_{x,y,z} + Vrms_{x,y,z}$$

$$Vrms = \sqrt{\frac{1}{N-1}\sum_{1}^{N}(V_i - Vmedian)^2}$$

With Vmedian= median value of all V components of the *N* neighbor vectors;

Vrms=deviation of V components of the *N* neighbor vectors.

This procedure has the advantage that large outliers at either end of the sorted list will not change the median value. This way is a reliable method for identifying and removing spurious vectors even when many spurious vectors are present, Westerweel [36].

7. Some 2D-PIV considerations

7.1. Interrogation window size

The size of interrogation window should be such that all particles within this cell have moved homogeneously in the same direction and the same displacement. As shown in Figure 35, the interrogation window size determines the sampling resolution and the smallest detectable flow structures.

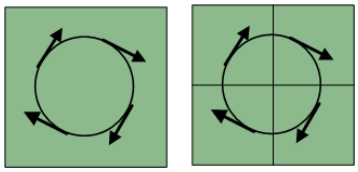

(a) (b)

Figure 35 Optimum size of interrogation window; **(a)** Interrogation window is too big (violation of sampling theorem), **(b)** Interrogation window is at the limit, but will do the measurement;

7.2. The particle displacement

As described, the fluid velocity is measured indirectly as a displacement of the tracer particles within a small cell in a finite time interval. The tracer particles are considered as ideal when they *i)* exactly follow the motion of the fluid, *ii)* do not modify the fluid properties or the flow and *iii)* do not interact with each other. It implies that the displacement field only provides an approximation of average velocity along the particle trajectory over a time Δt, as illustrated in Figure 36.

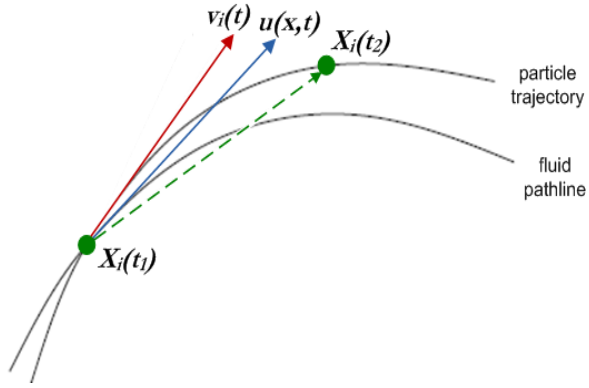

Figure 36 The particle displacement approximates the fluid velocity;

Thus, the particle displacement $\Delta \boldsymbol{s}$ cannot lead to an exact representation of $\boldsymbol{u}$ (the local fluid velocity) but approximates it within a finite error ε:

$$|\Delta s - u.\Delta t| < \varepsilon$$

The associated error is often negligible only if the spatial and temporal scales of the flow are larger in comparison to the PIV spatial resolution and the exposure time delay, and if the dynamical response of the tracer particle is fast [37].

7.3. Peak-locking effect

Sometimes, the velocity calculated has a bias toward integer values, which is called peak-locking or pixel-locking effect. It can be identified by zigzag type patterns in the vector field. It can also be better quantified by histogram plots of the pixel displacement. Peak locking can occur when the particle images produced on the imaging sensor are less than one pixel in diameter. The particle image diameter of 2-3 pixels assures avoiding this bias error, since 3 points yield most information for subpixel estimator then, for example, Gaussian function are successfully applied for the curve fitting.

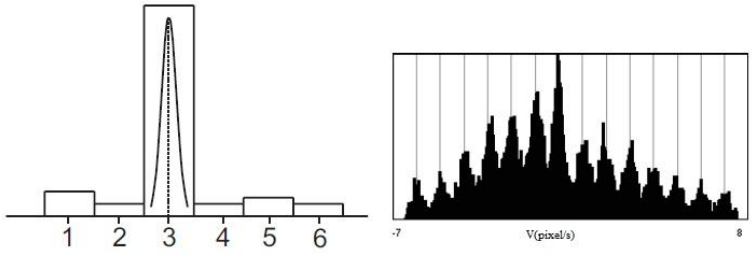

(a) A particle image size smaller than 1 pixel causes a strong bias to integer values

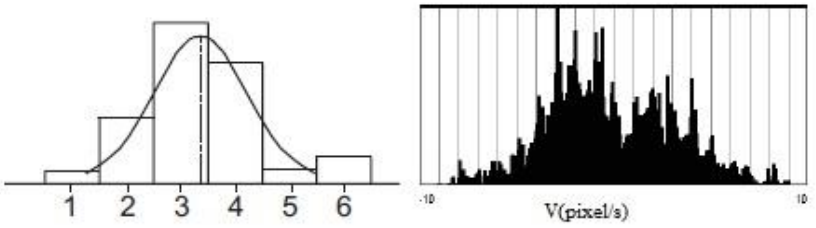

(b) A particle image size of 3 pixels assures avoiding peak-locking

Figure 37 Peak-locking effect, with permission of LaVision GmbH;

7.4. Accuracy of the PIV measurements

First of all, because of optical imperfections the recorded particle images are not perfect circular. Therefore, measuring the displacement of particle images is uncertain due to the irregular shape of the image particle. This uncertainty is proportional to the mean diameter of the particle image.

$$\sigma_{\perp x} = c_{\tau} . d_{\tau}$$

Where c_τ is a constant that depends on the ability of the analysis procedure to determine the displacement between the images. This constant is 1-10% [38].

Two major forms of error in PIV are the mean-bias and random errors (σ). These values are under influence of many factors. The PIV data processing with cross-correlation function and the sub-pixel interpolation is fundamental in the PIV accuracy. The analysis of PIV method with the cross-correlation approach using simulated images (normally done through Monte Carlo simulations) has shown that both the mean-bias and random errors have been found to be of the order of 0.1 pixels [38]. The accuracy of 2D PIV in optimal conditions is on the order of 1-2% that is commonly mentioned in literature. These errors in PIV measurements also depend considerably on how the experimental parameters are set e.g. seeding, resolution, time between pulses, light sheet thickness and alignment between the light sheet and the field of view where the measurements is performed. Still, the total uncertainty of PIV is often given about 5% in the best case.

7.5. Spatial resolution, dynamic velocity range and dynamic spatial range

Typically, the spatial resolution of a planar PIV is of order one millimetre and an appropriate width of the field-of-view in the flow is of the order of 100 mm. However, both larger and smaller fields are possible, subject to certain practical limitations. Although a PIV system is often characterized by its accuracy and spatial resolution, two quantities of dynamic velocity range and dynamic spatial range better describe the capabilities of a PIV system, especially in turbulence measurements. The dynamic velocity range is defined as the ratio of the maximum velocity range that can be measured with a fixed set of instrumental parameters to the minimum resolvable velocity measurement. The dynamic spatial range of a PIV is defined as the ratio of the field-of-view in the object space to the smallest resolvable spatial variation. Fundamentally, this ratio is the same as the number of independent vector measurements that can be made across the linear dimension of the field-of-view. Obviously, large dynamic spatial resolution allows one to measure small scale variation embedded in larger scale motion as occurs in numerous fluid mechanical phenomena such as boundary layers and turbulence. Dynamic spatial range is related to spatial resolution, and dynamic velocity range is related to the fundamental velocity resolution and accuracy of a PIV. The dynamic velocity range (DVR) is given by [35]:

$$DVR = max\,\Delta x_p / c_\tau d_\tau$$

Where $max\,\Delta x_p = u_{max}/\Delta t$, u_{max} is the full-scale velocity defined to the maximum magnitude of the flow velocity.

If the format of the recording medium is denoted by its dimensions L in the recording plane, then the field-of-view in the flow is given by $l=L/M_0$ based on optical arrangement. The minimum resolvable scale is less than $max\,\Delta x_p$, thus the dynamic spatial range (DSR) is at least[35]:

$$DSR = L/max\,\Delta x_p$$

The following equation describes the capability of a PIV system to have both a large dynamic velocity range and a large dynamic spatial range [35].

$$(DVR)(DSR) = L/c_\tau d_\tau$$

The format length L characterizes the size of the recording medium, which determines its capacity to hold information. The recorded particle image diameter d_τ is a measure of the performance of the optical arrangement and the optical imaging system, and c_τ is a measure of the ability of the interrogation algorithm to measure displacements accurately. PIV systems having large values of $L/c_\tau d_\tau$ are well suited

for turbulence research, and the measurement of the flows with higher Reynolds number require larger values of this constant.

7.6. Systematic error caused by viewing direction

Usually the camera should be set up so that the viewing direction is normal at the middle of the object plane. Even for this ideal arrangement, a slight distortion at the edges of the recorded image is always present, depending on the distance to the object plane, and the magnification factor, Figure 38.

Figure 38 Systematic error caused by viewing direction;

When the difference of the viewing angle at the edges of the image relative to the normal direction is less than 8°, the error of displacement measurement will be less than %1 (*1-cos(8°)*). For example, if the field-of-view is 10 cm at a distance of 50 cm from the camera, the inclination of the viewing angle at the rim will be *arctan(5/50)≈5.7°*. This means that a displacement of 10 pixel at the edges of the image is actually measured as 9.95 pixel. Since such (locally constant) error of 0.5% is rather small, we can simply ignore it. However, if the field of view is bigger (for example 20 cm) at a closer distance to the camera (for example 20 cm), the error increases (above 10% for the viewing angle of 30°). Therefore, one should at least be aware of this error and check the configuration for a given experimental setup.

If the experimental setup requires a viewing angle significantly different from the normal direction, a correction procedure is mandatory to be able to calculate correct results.

8. Optimum 2D-PIV configuration

We now consider an optimum PIV configuration for a given experiment. The most important consideration is to match the size of a typical particle image with the resolution of the recording medium, denoted by d_r . If the image diameter satisfies the criterion of $d_e \geq 2\, d_r$, the finite resolution of the recording medium has a negligible effect on the accuracy of measuring the displacement of the particle

image. The optimum magnification and the corresponding optimum *f*# can be found as the following for an optimum optical arrangement [35]:

$$M_{optm} = \frac{2d_r}{\sqrt{(1.5\delta_z\lambda + d_p^2)}}$$

$$f\#_{optm} = \frac{0.5\sqrt{(\delta_z/\lambda)}}{1+M_{optm}^{-1}}$$

The experiments in water instead of air require larger tracer particles to compensate for scattered light energy lost due to the smaller ratio of refractive indices. The recorded particle image of a 20μm particle is less sensitive to the effects of parameters other than the geometric image diameter, so the optimum magnification varies less for experiments in water.

9. Particle Tracking Velocimetry (PTV)

PTV is a well-established technique (even before PIV) to determine the velocity of individual tracer particles embedded in flow by tracking them in video recordings or successive image frames. Their trajectories are derived from running discrete visualizations of the flow, and PTV is, therefore, considered as the low-density range of PIV that deals with the correlation evaluation to estimate the local motion of the tracers within interrogation windows, as already described. When locally strong velocity gradients with small vortices are present across the interrogation area, PTV will resolve the corresponding vectors of changing magnitude, whereas PIV will yield an averaged vector with lower accuracy due to the broadening of displacement peak.

PTV essentially consists of two parts: *i)* identification of the particles in a given frame, and *ii)* matching of these particles with the corresponding particles in the successive frames. Therefore, PTV measurements contain two main sources of error: the error in determining the particle positions in images and erroneous particle pairing. The first one is related to the imaging itself and the adopted image processing algorithm. The PTV measurement contains velocity errors that are mostly related to the rough estimate of the particle centroids. If the locations of the particles have been reliably determined, the subsequent matching process aims to find the corresponding particles in the next frame. The purpose of the matching procedure is thus to determine the correct link for the same particle from one image frame to the next one. Obviously, this can only be a path with a maximum likelihood for a specific criterion. The three basic tracking principles can be summarized as follow, Pereira et al [39]: estimating the position of the selected particle in the next image frame; determining a neighborhood area around the

expected location in which the particle is likely to be found; applying appropriate criteria to determine the most likely track if there is more than one possible option. These principles can be applied to any flow regime under consideration and can be extended to any tracking task in which moving objects must be tracked in time.

The simplest approach to match corresponding particle images is the nearest neighbor method. The link criterion in this method is simply the minimum distance of a match or the minimum variation of length and angle of all possible tracks of an object particle in a search radius of the neighborhood. In this method, multi-frames in a tracking line are usually used for the evaluation of the smoothness of a particle trajectory and accurately measuring the particle velocity. Classical algorithms for PTV have been introduced by Kobayashi et al. [40], Nishino et al. [41], Hassan and Canaan [42], and Malik et al. [43]. An inherent challenge for these algorithms is the compromise between accuracy and computational cost. In addition, the nearest neighbor methods are effective for relatively low-density particle images in which the particle displacements are smaller than the mean inter-particle distance. A potential weakness of these algorithms is also that they search for the minimum travel distance only from possible matches within a localized search area, and hence the searching is not performed throughout the image. Therefore, a global minimum is not sought.

Okamoto et al. [44] presented their two-frame model in which particle pairs were identified by searching for the smallest spring force calculated over particles in a certain neighborhood. Another method with the view to improve the detection of particle pairs to achieve applicability in higher density particle images is the use of a predictor. This predictor can decrease the search area significantly in the next frame and thus improve the match probability of particles. Such predictors can be either theoretically known velocity distributions or experimentally obtained by PTV of previous images or a coarse PIV evaluation (super-resolution PIV). One typical example of this is the hybrid PIV/PTV method introduced and used by Keane et al. [45], Cowen and Monismith [46], Takehara et al. [47], and Cardwell et al. [48], in which standard cross-correlation PIV is employed prior to the individual-particle tracking in order to estimate in advance the local velocity to be calculated by PTV. Another example is the hybrid PIV/CFD method, see Kaga et al. [49]. This approach is also used in most of the tracking algorithms that use multi-frames. After the first step, every next step is using the velocity vector to predict the position of the particle in the next frame. However, a problem with these improved schemes is that they are not always practical.

The probability match/relaxation method is another scheme of two-frame particle tracking. The fundamental idea of this method is the search for the most

probable link of a reference particle while assuming similar displacements for its neighbor particles, i.e. so-called quasi-rigidity. The algorithm proposed by Baek and Lee [50] and Ohmi and Li [51] for tracking discrete particles is based on the iterative estimation of the match and no-match probability as a degree of the matching. In an iterative process in order to achieve successful termination of the tracking algorithm, the correct link probability, namely match probability, is gradually increased close to unity while the other probabilities, no-match probability, tend to zero. The match probability algorithm mainly relies on quasi-rigidity conditions applied to the neighbor particles. The threshold for the maximum velocity implies that the corresponding particles cannot move beyond the maximum expected displacement in the flow field. The heuristic conditions of quasi-rigidity are usually explained as small velocity changes and coherent motions. Since the particles have a finite mass, small velocity changes are a natural consequence of the physical law of motion. It is also anticipated that a group of particles within a small region move coherently, namely represents a pattern of common movement in successive images. These requirements restrict the applicability of the algorithm although the other techniques such as correlation in PIV or three/four frames PTV also assume implicitly that these requirements are valid [50].

The third approach to the particle-matching algorithm is Artificial Neural Networks (ANNs). Knaak et al. [52] proposed a Hopfield neural network in which a cost function involving the fluid dynamics constraints is minimized to solve the particle correspondence problem. The approaches such as nearest neighborhood or relaxation method are inherently treated as a local minimization of a cost function that involves the underlying constraints and not the whole of constraints. Using neural networks, e.g. Hopfield networks, all constraints can be explicitly included in the cost function in a computationally efficient manner. The cost function that Knaak et al. used is the summation of four terms, neighborhood criterion, the uniqueness constraint, the rigidity constraint, and the smoothness constraint, derived from the physics of fluids. Hopfield neural network proposed is an $N \times M$ array of neurons where N and M are the total number of particles in the first and second image, respectively, to minimize the cost function formulated in order to solve the problem of particle correspondence in PTV. Their network performed much better than the nearest-neighbor algorithm. The neural network proposed by Grant and Pan [53] for pairing is different from the above. It implements a filter that, when applied to the particle images, lets pass through only those that match. Ohmi and Sapkota [54] showed that a Cellular Neural Network can be successfully implemented in a particle pairing algorithm of PTV with remarkably low computation time and adequate accuracy. The Labonté algorithm was inspired by

Kohonen's Self-Organizing Map (SOM) neural network [55]. It consists of two sub-networks, each one associated with one of two successive frames. The weight vectors of their neurons start at the positions of the particle images in the associated frame. The network dynamics makes these weight vectors follow trajectories that approximate those of the positions of the particles in the two frames. The weight vectors from the two sub-networks that correspond to matching particles meet at some midway points between them while those that correspond to unmatchable particles stay alone. This neural network can be regarded as a pre-sorting routine for the nearest neighbor method, for which the weight vector of a given particle acts as an initial indicator pointing towards the matchable partner. Labonté described his procedure as an enhanced version of the nearest neighbor-matching algorithm. He showed that his SOM algorithm iteratively converges towards a solution even when the number of matching particles is low. The algorithm was found to require only a few correct matching pairs to progressively adjust itself. A striking feature of this algorithm is that its learning principle seems to correspond perfectly to the intuitive recognition of particle matching through the eyes of humans. Others have also developed the algorithm of particle pairing based on Labonté SOM neural network in 3D PTV, e.g. Ohmi [56] and Ohmi et al. [57].

10. Techniques of phase separation in two-phase flow measurement

The following four different fundamental techniques can be found in literature where PIV/PTV has been applied to the simultaneous measurement of both phases of two-phase flows and needed discrimination between flow tracer particles and dispersed phase: 1) fluorescence tagging, 2) amplitude discrimination, 3) phase dynamics, and 4) geometrical characteristics.

Fluorescent particle tagging is one of the most mature of phase separation techniques, and commercial systems are even available[58]. Using this method, one phase (usually tracer particles) is labeled with a fluorescent dye that can be excited by the light source (e.g. Rhodamine). The dye absorbs the incident light, then re-emits at a longer wavelength. This makes it possible to discriminate the PIV tracers from other scattering objects, such as bubbles, droplets, and dispersed particles as second phases. It needs an appropriate optical filter to block the light with the wavelength of light scattered and passes the fluorescent light. Therefore, two cameras are usually used; one which records light directly scattered by both phases, the other which only records fluorescent images. The emitted fluorescent light is isotropic that means there is no dependency of particle-image brightness on the light beam direction and viewing angle. It only depends on the amount of fluorescent dye. The use of two synchronized cameras and the need of a powerful

laser to produce adequate intensity fluorescent images are drawback to this method. This technique has been extensively used for the study of bubbly flows.

Amplitude discrimination techniques count on a strong difference in the light scattering amplitude between the dispersed and carrier phase particles to separate the phases. Therefore, the maximum scattering cross-section of the tracers of the carrier phase and the smallest particles of the dispersed phase are required to be different by more than an order of magnitude to prevent significant crosstalk between the phases. Even with properly selected seeding particles, this method requires careful tuning and patience to optimize the imaging to eliminate the interference between the phases.

Phase dynamics technique was established upon the inherent differences in the motion of the two phases to discriminate between them [59]. The separation is performed in correlation map by identifying the two dominant correlation peaks, one that represents the motion of the tracers while the other provides the displacement of the dispersed phase. This method can be useful for high concentration flows of very fine particles and can even provide carrier phase turbulence statistics. However, because the method is based on the bulk average motion of the dispersed phase, the details of the interaction terms may not always be clear.

The fourth class of techniques is based on the geometrical properties of the dispersed and seeding particles to separate the phases. The one can use a particle mask function to eliminate the crosstalk between the phases from influencing the correlation calculations. The masking uses a threshold calculation of the particle's size, and hence a significant difference between the sizes of the particles is required for proper separation. The other method in this class was developed by Kiger and Pan [60]. They provided a reliable, single camera technique using a median filter. A median filter is a nonlinear signal processing technique that has been found effective in reducing random noise, also called salt-and-pepper noise because of its appearance as dots superimposed on an image, and periodic interference patterns without severely degrading the signal [61]. In PIV image processing, the property of preserving sharp edges makes the filter useful because it allows more information about the original image to be maintained. This is especially beneficial in regions of high shear, where the ratio of signal to noise is relatively low. For a two-phase image with both small tracer particles and large particles, the tracers can be regarded as salt-noise scattered over a uniform background. This technique can resolve the local particle/fluid interaction within the flow, and the performance of the separation process can be quantified as a function of the particle size and image resolution.

Chapter 3

FIBER TRACKING

In combined PIV/PTV measurements of particle-laden flows, the measurement of the dispersed particle-phase motion is carried out by a PTV approach. The algorithms of PTV have inherently been designed for the low-density range of tiny particles of flow tracer. In case of particle suspension, if the particle concentration is low enough to avoid a large number of overlapping particle images, the particles can be identified with reasonable accuracy. However, a lack of consistent technique to match particles in the successive images makes still tracking difficult. The condition of quasi-rigidity, which relaxation methods are based on, is not appropriately applicable to follow individual particles scattered in the fluid phase. Furthermore, it is likely that we lose many matchable particles (information) using nearest neighborhood methods with multiple successive frames due to out-of-plane losses. Besides, in the case of a concentrated particle suspension the nearest neighbor method is not efficient.

A. Carlsson et al. [62] have proposed a steerable filter to determine position and orientation of fibers in digital images of flowing suspension with acceptable error. Therefore, here a novel two-frame algorithm was developed to take the fiber orientation into account for pairing as well as their positions for tracking rod-like fibers in suspension flows. Using one additional characteristics of the particle will improve not only the robustness against loss of pair-particles between image frames but also reliable matching for larger numbers of dispersed particles. Neural networks are one of the most attractive algorithms for the particle-matching problem of PTV since they do not require any prior information of the flow field and particle behavior examined. Moreover, the searching to find particle pairs is performed globally; see [53], [52], [55], and [56]. Among neural networks, the Self-Organizing Map (SOM) model seems to be a convenient tool for the present purpose because it is an unsupervised learning model that is capable to group similar particles only based on particle features in the images. The two-frame algorithm that it is presented here is based on SOM neural network in order to satisfy the requirements mentioned above.

1. Introduction to the concept of Artificial Neural Network

It is believed that the human brain consists of a three-dimensional matrix of interconnected processing units, called neurons that have the capacity of implementing simultaneous and non-linear processing strategies. A biological neuron has four types of components that should be considered in understanding an artificial neuron: dendrites, synapse, soma, and axon. The neuron's dendrites are responsible for receiving signals from other neurons. The signals are electric impulses that are transmitted across a synaptic gap via a chemical process. The action of the chemical transmitter modifies the signal in a manner similar to weighing them. The synaptic connections between the neurons hold memories which can be updated both during the learning (initializing) stage and processing of data sets. The soma, or body of neuron, collects the incoming signals. When sufficient input signal is received, the cell sums or integrates the inputs and then acts as a processing unit in which it either triggers, giving an electrical output, or stays inactive. Its signal is transmitted through its axon to the other neurons, [63]. The described nature of the processing elements is used in many artificial neural networks. As shown in Figure 39, the neuron model may be considered as a multiple input, single output operator. The x_i is the input signals from other neurons, the w_i is the interconnection weights, and y is the output signal. Each input x_i is multiplied by its corresponding weight w_i, and then the product $x_i.\ w_i$ is fed into the neuron. In the neuron, these products is summed up so that this summation usually denoted as net in the literature. In mathematical form for two vectors input $X=(x_1, x_2, ..., x_m)$ and weight $W=(w_1, w_2, ..., w_m)$, *net* is the dot product of these two vectors, $X.W \equiv x_1w_1+x_2w_2+...+x_mw_m$. Finally, the neuron computes its output as a specific function of net, $y=f(net+bias)$. This function is called the activation function that can be defined in different forms depending on the characteristics of applications. A neuron can be considered as a black box, which receives input vector X and generates a scalar output y.

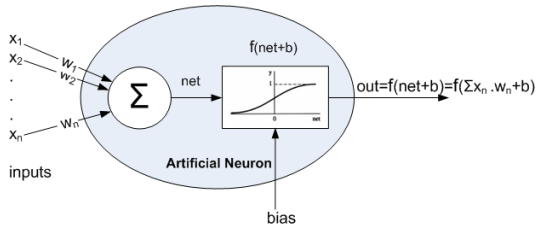

Figure 39 Artificial neuron model;

An artificial neural network is characterized by *i)* the architecture of interconnection of its neurons, *ii)* its activation function, and *iii)* the method the

weights of the connections is modified, called training or learning. The architecture of a network comprises of distinct layers of neurons, a layer of input neuron that receive signals from the outside world, a layer of output neuron from which the response of the net can be sent out, and any number of hidden layers between them, as shown in Figure 40.

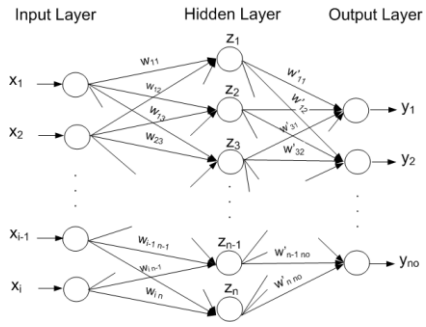

Figure 40 A typical network architecture;

In some other neural network models, output of neurons can also feed backward. A neural network in which the outputs can propagate in both forward and backward directions is called recurrent model.

The most valuable property of a neural network is the ability to learn, the process the neural network adjusts its weights in response to external inputs. The process of learning is categorized to supervised and unsupervised learning. Many neural network models have been developed for different applications. The most functional networks are:

I. The back propagation network is a multilayered, non-recurrent, supervised learning model and is used mainly to recognize input patterns with pre-defined classes.

II. The Kohonen self-organizing maps network is a two layered, non-recurrent, unsupervised learning model that is capable to cluster patterns of input without knowledge of their distribution.

III. The Hopfield neural network that is a form of a non-multilayered, recurrent, supervised learning models works differently from the other network models. The architecture of this network creates an internal state that allows exhibiting dynamic behavior and can use their internal memory to process arbitrary sequences of inputs. In Hopfield neural network, a cost function derived for a specific case mathematically to describe the system is optimized.

IV. The ART (Adaptive Resonant Theory) network is also an unsupervised learning model used to classify input patterns.

The capability of neural networks in modeling complex nonlinear problems as well as providing a fast, automatic method in some applications in fluid mechanics and heat transfer have proved, [64], [65] and [66]. The analysis of PIV/PTV images typically involves feature extraction and classification. Indeed, the nearest neighbor and statistical analysis methods have been used to group the particle images for quantifying the local displacement in track of particle image. Generally in a neural network used in classification, the samples may be classified using pattern recognition rules established on training data sets or clustering by self-learning, where one wants a neural network to group data by similarity. The neural networks have been used for recognizing pairs to improve the efficiency of analysis.

1.1. Kohonen Self-Organizing Map

The self-organizing map neural networks introduced and developed by Kohonen [67] assumes a topological structure among the cluster units. It actually converts complex and nonlinear statistical relationships between high-dimensional data into simple geometric relationships on low-dimensional maps. This property can be observed in the brain, but the other artificial neural networks do not have this. Self-organization is an unsupervised learning method that the neural network organizes itself to form useful information in a competitive learning procedure in which neurons compete with each other. The winners of the competition strengthen their weights while the losers' weights stay unchanged or are weakened. The architecture of the Kohonen network is a two-layer network, as shown in Figure 41. The first layer is the input layer, and the second one is the output layer, called the Kohonen layer and the neurons in the Kohonen layer are called Kohonen neurons. Every neuron of input layer is connected to all Kohonen neurons, with a variable associated weight. The network is non-recurrent, and information is fed forward only from the first layer to second.

The weight vector for a cluster unit serves as a sample of the input patterns associated with that cluster. During the self-organization process, the cluster unit whose weight vector matches the input pattern most closely (typically Euclidean distance) is selected as the winner. The winning unit and its neighboring units, in terms of the topology of the cluster units, update their weights. Finally, the network clusters the n-inputs to m bunch units.

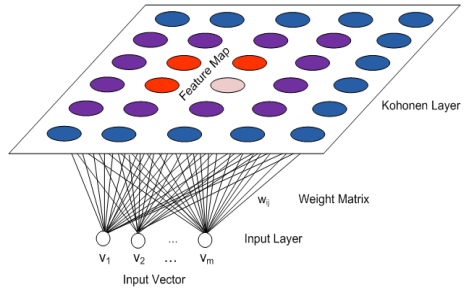

Figure 41 SOM neural network;

2. SOM implementation for pairing

The method used in the present study is primarily based on the SOM model introduced by Labonte´ [55]. However, improvements have been made in order to take the particle orientation into account and also to enhance the algorithm performance.

The network architecture comprises two similar sub-networks, each one corresponding to one of the two images. Each of the sub-networks has one layer of neurons of which the initial weight vector is the same as the characteristic vector of the non-spherical particle in images, (x,y,θ), where x, y and θ are the normalized components of particle position and orientation in the image respectively. Thus, each neuron is associated with an individual particle. Within each sub-network, the neurons are interconnected so as to allow a winner to take all competition among them. Here, the variables related to the first and the second image will be denoted with small and capital letters, respectively. Let v_i $(i = 1,\ldots,N)$ and V_j $(j = 1,\ldots,M)$ be the characteristic vectors of the particles in first and second image ($v_i=(x_i,y_i,\theta_i)$ and $V_j=(x_j,y_j,\theta_j)$) as inputs to sub-networks, where N and M are the number of particles in the first and the second image respectively. Each neuron has a weight vector, $w(x,y,\theta)$, represented by w_i: $i=1,2,\ldots,N$ and W_j: $j=1,2,\ldots,M$ for the first and second sub-network.

Both sub-networks react similarly to their inputs. At the beginning, we set the initial weight vectors of each neuron equal to the characteristic vector of the particles in the images. Therefore, the first sub-network has N neurons located at v_i and the second one has M neurons at V_j. The weight vectors are updated so that the stimuli for one sub-network are the weight vectors of the neurons in the other sub-network. Let $\|a-b\|$ denote the Euclidean distance between the two points a and b in vector space, as $||a-b|| = \sqrt{(x_a-x_b)^2+(y_a-y_b)^2+(\theta_a-\theta_b)^2}$. First, the input vector v_i is presented to the second sub-network. Then, an activated neuron is selected from the latter sub-network, which is the one with the weight vector closest to v_i and if $\|\mathrm{w_j}-\mathrm{v_i}\|<D_{max}$. D_{max} can be chosen in a trial-and-error process to

reach high performance in matching for a few test images. It can be explained as the largest length of the possible Euclidean distance in the images (limitation of similarity) like the limitation that is used in many other tracking algorithms. However, we should consider that here the algorithm actually seeks the activated neuron and the winner in the entire image. When the first sub-network is stimulated with the weight vector W_j of the activated neuron of jth in the second sub-network, neurons compete and the one with the minimum distance (the closest) and the condition of $\|w_i - W_j\| < D_{max}$ wins the competition. If there is no activated neuron, there is no competition, and when there is no winner, there will be no weight updating. When there is a winning neuron, the winner and its neighbors within a certain distance "*R*" are awarded a weight change. If "c" denotes the winner's index, and "α" is a relaxation factor between *0* and *1*, each neuron of the first sub-network is subjected to the following change of weight vectors:

$$\Delta w_i(c_j) = \acute{\alpha}(W_j - w_c) \qquad where \qquad \acute{\alpha} = \begin{cases} \alpha & if \ \ ||v_i - v_c|| < R \\ 0 & otherwise \end{cases}$$

First, the radius *R* of the winner neighborhood is set so large that many neighboring neurons are included in the network. Once the weights have been updated, the neighborhood radius *R* is decreased to a smaller and smaller size, and eventually sufficiently small to include only the winner. The weight vectors of the first sub-network are updated according to:

$$w_i \leftarrow (w_i)_{old} + \sum_{j=1}^{M} \Delta w_i(c_j) \qquad (i = 1, \dots, N)$$

In the next step, in turn, the stimulus vector w_i of the *ith* neuron activated by V_j in the first sub-network is presented to the second sub-network. A winning neuron is selected as the closest one to w_i and the condition mentioned. Similar to the previous step, each time the weight vector w_i is presented to the second sub-network, the weight vectors of the second sub-network are updated according to:

$$W_j \leftarrow (W_j)_{old} + \sum_{i=1}^{N} \Delta W_j(c_i) \qquad (j = 1, \dots, M)$$

The alternate cycles described above are repeated iteratively until the two sets of weight vectors reach together into one point while the two sub-networks react to each other. A small range ε has to be determined, within which two weight vectors will be considered to be equivalent. In a final computation cycle, if the two weight vectors of sub-networks are less than this small threshold distance ε, the matching pair is accepted; otherwise, it is discarded because their relationship is apparently not close enough.

2.1. Test cases

It is practically impossible to assess the performance of the algorithm using laboratory data. Hence, the proposed algorithm is examined by means of both 2D synthetic images of ellipsoidal particle suspension flow and results of a direct numerical simulation (DNS) of prolate particle-laden turbulent channel flow. An advantage of these synthetic images or the results from DNS is that we can refer to the original particle displacement data, from which the images are generated, and compare particle-tracking results directly.

-Matching performance parameters

In this section, it is explained some general parameters on which the achievements of the tracking depends. Because the position and orientation of the particles are known, number of particle pairs and their displacement are also known in advance in the test cases. The particle number density is defined as the following:

$$\rho_o = \frac{\int P(r)dr}{A_o}$$

Where *P(r)* is the probability density function of a particle with radius *r*. The number of particles within the observation area A_o is simply given by:

$$N_o = \rho_o . A_o = \int P(r)dr$$

The mean inter-particle distance, corresponding to the probability of finding a single particle within a circle, can be obtained as:

$$d_o = \sqrt{\frac{1}{\pi . \rho_o}}$$

Here, the tracking parameter that influences the performance of any tracking algorithm is defined as:

$$\emptyset = \frac{d_o}{s_{mean}}$$

Where s_{mean} is the mean particle displacement in the images. We also introduce the recovery ratio and the mismatch ratio to evaluate the performance of the algorithm:

$$\eta_r = M_{cl}/N_{cl} \qquad \& \qquad \eta_m = M_{sl}/N_{fl}$$

The recovery ratio η_r is the number M_{cl} of links correctly found divided by the actual number of correct links N_{cl}. η_m is the mismatch ratio defined as M_{sl}, the number of spurious links, divided by N_{fl}, the total number of links detected by the algorithm including both correct and incorrect links. Thus, η_r represents a direct measure of the performance of the algorithm while η_m indicates a noise-to-signal

ratio and indicates if the algorithm can reliably discriminate and dismiss unpaired/noise particles.

-Test case of plane potential suspension flow in a corner

The artificial images considered here are from an idealized case in which ellipsoidal particles follow a pattern of plane potential flow in a 90° - corner. Although this does not correspond to a real situation, they provide a high complexity to match, i.e. from short to long displacements as well as the change of orientation of a particle between two successive snapshots. It is considered three different concentrations 50, 100 and 200 particles within an image dimension of 2016×2016 pixels that is a standard size in PIV/PTV measurements. In constructing the images, to take into account the particles moving in and out of the window due to the fluid motion in the plane, the particles were randomly distributed in an area 10% larger than the main interrogation window. Then we let all these particles undergo the displacements corresponding to the flow pattern in the next image and those that were still in the main window were provided as the particles in the successive images. In addition, in order to model the particles that would enter or leave the measuring domain due to moving perpendicular to it in a real flow, we added 20% unmatchable particles distributed at random positions as noise.

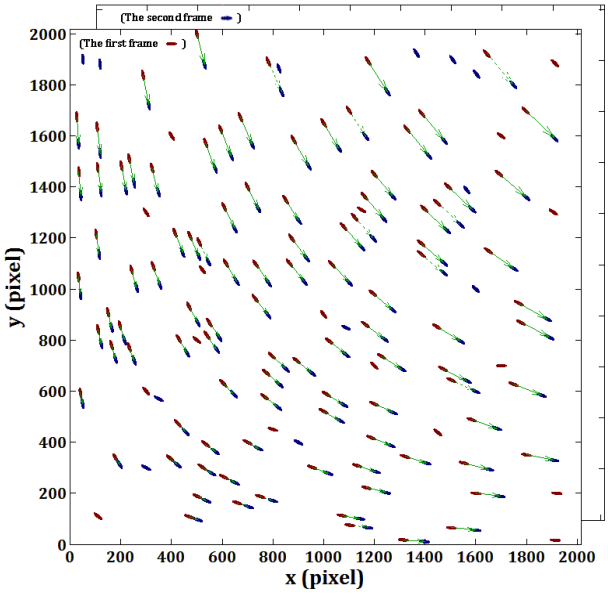

Figure 42 Superposition of two successive snapshots of non-spherical particle suspension flow; (●)the red particles in the first snapshot; (●)the blue particles in the second snapshot that undergo the displacements corresponding to plane potential flow pattern in a 90° corner; the dotted green arrows are the original and known match links, the solid green arrows are those that the algorithm could find;

Figure 42 shows a superposition of two successive frames for the case of 100 matchable particles in the plane potential flow in a 90° corner. As seen, the algorithm found 83% of match links, and it could even detect corresponding particles where the particles displacement exceeded the inter-particle distance. The algorithm could also distinguish between dissimilar particles situated in the vicinity of each other since their orientation angles also were considered.

The performance of the algorithm for this test case is reported in Table 1 for all three cases of different particle concentrations in the image. The tracking parameter ϕ is varied from 1.75 to 0.87 with increasing particle concentration from 50 to 200. The number of epochs, i.e. the computational cycles in which the weights are varied, is fixed to 12 for all cases, and the updated weights of the two subnets converge to corresponding one during this period. As seen in this table, the computational time and efficiency of the algorithm depends on the particle number and accordingly on ϕ. In the case that the mean inter-particle space is less than the mean particle displacement (ϕ=0.87), the recovery ratio η_r is severely decreased to 64%. The mismatch ratio η_r is increased to 30%, but the performance of the algorithm is still reasonably acceptable. This algorithm was also compared with an particle-tracking code developed based on the nearest neighbor method from reference of [68]. This code was applied to the same three synthetic cases, and the results are also shown in Table 1. The performance of the two algorithms is equally suitable for the dilute case. However, when the particle concentration is increasing, the efficiency of the nearest neighbor algorithm is decreasing. For all particle concentrations, the present algorithm is better than the nearest neighbor algorithm. For the highest concentration, the present algorithm is superior.

Table 1 The algorithm performance for the cases of synthetic images

Possible pairs (N_o)	ϕ	The SOM-based algorithm			The nearest neighbor algorithm	
		η_r	η_m	Computational time	η_r	η_m
50 particles	1.75	%90	%8	0.66 (sec.)	%88	%10
100 particles	1.3	%83	%11	0.76 (sec.)	%67	%29
200 particles	0.87	%64	%30	2.1 (sec.)	%24	%65

-Test case of prolate spheroids dispersed in wall turbulence: An example of real 3D data from DNS

We also estimated the performance of the algorithm by tracking dispersed prolate spheroidal particles in a turbulent channel flow obtained from DNS. This serves an example of a real case of usual combined PIV/PTV measurements of turbulent suspension flow.

The direct numerical simulation results of fully-developed turbulent channel flow laden with elongated ellipsoidal particles are available for particle aspect ratio 5:1 and dimensionless response time τ^+=30 at a friction Reynolds number $Re\tau$=180 (based on the half channel width h), see [31]. The computational domain was 6h×3h×h in the streamwise, spanwise, and wall-normal directions, respectively. We are thus able to examine the present algorithm by tracking particles dispersed by the turbulence of the carrier fluid. The particles was just considered that traveled through a narrow volume of 2h×1h×0.02h in the middle of the channel at a distance z^+=30 from the channel wall, i.e. fairly close to where turbulent velocity fluctuations are most intense, and the particle orientations vary considerably. This volume corresponds to a conventional observation volume in PIV/PTV measurements. The projection of the particle motion and orientation on the *x-y* plane parallel to the channel walls was extracted. Indeed, this DNS-based test case provides a physically realistic distribution of non-spherical particles in wall-turbulence including all appearing or disappearing particle images in the measurement domain due to out-of-plane fluctuating motions. Therefore, the data set includes 2D motion and orientation of the prolate particles in a wall-parallel plane. In this case, the initial number of particles in the field of view, *No*=122, is unchanged, and the mean inter-particle distance is thus constant with *do*≈73 pixels. The tracking parameter ϕ was varied by choosing different time intervals, $\Delta t^+ = \Delta t\, u_\tau^2/\upsilon$, hence changing the mean particle displacement as provided in Table 2. The epoch number (number of iterations) for all these test cases is fixed to 20, and the computational time was in the order of 1.0 s. An illustrative example of ellipsoidal particles scattered by the numerically simulated turbulence of the carrier fluid at two consecutive frames with a time interval of Δt^+=0.096 is shown in Figure 43.

Table 2 Tracking parameter and mean particle displacement for different values of Δt^+; *do* ≈ 73 pixels;

Δt^+	s_{mean} (*pixels*)	ϕ
0.012	8.56	8.53
0.024	17.1	4.27
0.048	34.2	2.13
0.096	51.35	1.42
0.192	68.5	1.07
0.384	85.6	0.85
0.768	102.7	0.71
1.536	119.82	0.61

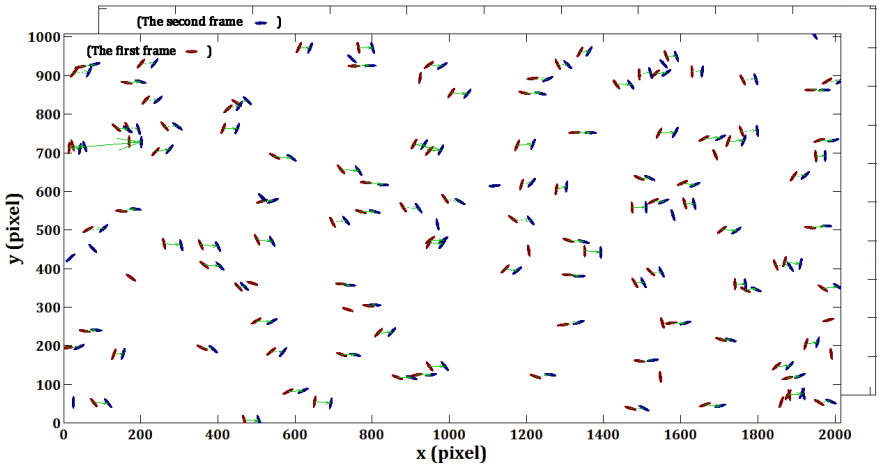

Figure 43 Superposition of two successive frames of prolate particles dispersed in turbulent channel flown resulting from DNS-based simulations, ϕ=1.42; the red ellipses are particles in the first snapshot; the blue ellipses are particles in the second snapshot; the dotted green arrows are the original and known match links; the solid green arrows are the ones detected by the algorithm;

Figure 44 shows the recovery ratio η_r and the mismatch ratio η_m as a function of the tracking parameter ϕ. It is seen that the recovery ratio decreases significantly to about 54% as ϕ reduces to 1.0, whereas the mismatch ratio η_m still remains low (less than 15%). This arises from the fact that an increased time step, which decreases ϕ, causes more diversity in the particles orientation and position due to the intense velocity fluctuations in this observation area. This high diversity leads to relatively low efficiency of the particle matching that is only based on feature extraction with no pre-estimated displacement. However, the low number of erroneous displacement vectors detected (η_m<15%) makes this algorithm reliable and robust.

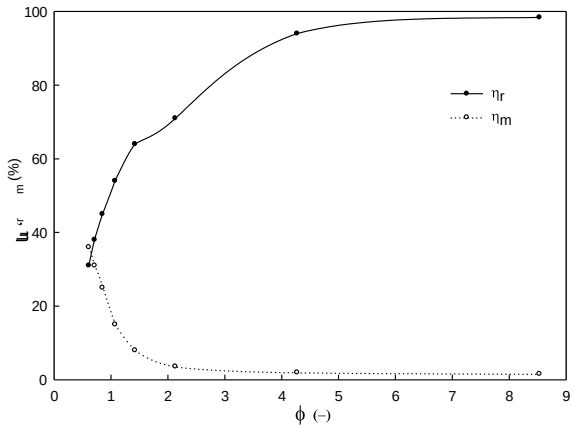

Figure 44 Particles dispersed in the wall turbulence case: recovery ratio η_r and mismatch ratio η_m;

Chapter 4

Experimental Facility and Material

The experiments were conducted in the water table facility at Linné FLOW Centre, KTH Mechanics Lab through combined PIV/PTV measurements. The well-known PIV technique was used for the measurement of fluid phase flow and some novel PTV techniques, described in the previous chapter, were applied to track fibers in the flow and to measure the motion of fibers. Schematic representation of the experimental setup and definition of the coordinates of x, y, z are shown in Figure 45.

1. Flow apparatus

The test section of the water table is made of glass plates with length 230 cm and width 56 cm. These dimensions promise fully developed turbulent flow and absence of any sidewall boundaries effects and disturbance due to the reservoirs on the flow over measurement area in the centre and at 130 cm distance from the start point of flow. Reservoirs are located upstream and downstream of the test section, Figure 45. Two upstream reservoirs are for mixing of the suspension and reducing disturbances in flow as settling chamber, respectively. The reservoir in downstream is to store suspension. The total suspension volume is 120 liters.

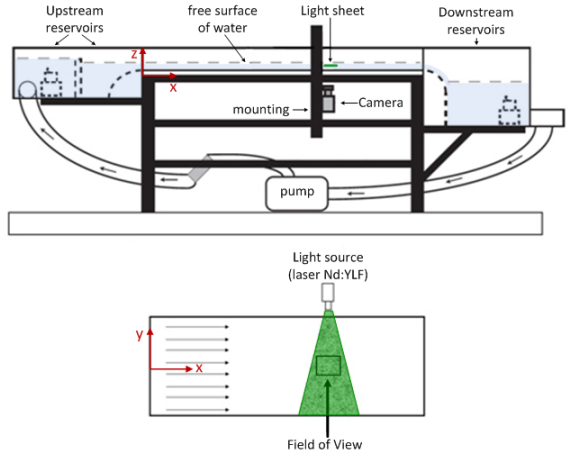

Figure 45 Schematic representation of experimental setup; the flow direction on the water table is left to right;

The angle of the test section with respect to the horizon is adjustable by a screw joined to stands. The film of suspension flows down, driven by gravity alone, on the slightly inclined table, and the suspension is pumped from the downstream tank to the upstream tank to make a closed circuit flow. The thickness of film flow for a specific angle of the test section is set by controlling the flow rate of the pump in order to attain a certain friction Reynolds number (Re_τ). With appropriate configuration of the pump setting and the table angle, we can establish a no acceleration condition for the flow over the test section.

2. Optical measurement setup

A single camera (Imager Pro HS 4M; double-frame 12 bit CMOS with resolution of 2016×2016 pixel and pixel size of 11μm × 11μm) and light sheet optics (with divergence: f= -10 mm and adjustable focus: 0.3 – 2 m) are mounted on a traverse unit. It makes possible to shift the light sheet and camera to a new position in two axes of x and z without changing their position with respect to each other. The camera was placed beneath the bottom wall of the water table in down to up direction at the location of the measurement area in order to record the images of flow on the table, Figure 45.

The measurements were carried out in planes parallel to the bottom wall, i.e. planes parallel to the x-y plane, illuminated using a Nd: YLF laser (Litron Lasers; double-exposure 22.5 mJ/pulse @ 527 nm) to create the field of view. The laser was set so that the waist of the light sheet was at the centre of the imaging domain with thickness of approximately 1 mm throughout the domain.

The camera lens (Sigma; 105mm f/2.8 Macro) was focused on the imaging domain at the fixed distance of 30 cm to have a field of view in size of 63 mm×63 mm in a magnification factor of 0.35. This size of field of view is appropriate both to capture sufficient number of coherent structures of turbulence and to have high resolution in the calculation of the velocity field. Because the water table walls are flat plates and the camera was installed normal to the middle of the object plane, we had almost no image distortion. Besides, since the field-of-view lengths were 63 mm at a distance of 300 mm to the camera, the deviation of the camera viewing-angle at the edges of the image from the standard perpendicular view in the middle of the image is $arctan(31.5/300) \approx 6°$. This means that the error in measuring displacement due to image perspective is less than 0.5%. The f-number of 5.6 was used to yield the optical depth of field of 0.98 mm. This depth of field is of the order of the light sheet thickness, and thus many out-of-focus effects are not expected. The reason for considering the depth of focus in combination with the light sheet thickness is to estimate the equivalent measurement volume, which has

to be considered when choosing the size of the interrogation window. Regarding to this PIV setup, the scaling factor was 0.0313 mm/pixel.

DaVis 7.2 (LaVision GmbH) did the hardware control, data acquisition and PIV processing. The flow was seeded by Glass Hollow Spheres (LaVision GmbH) with a mean size 9-13 μm as tracer particles.

The camera recorded the images with double frame-double exposure in the interval of 700 μs. This delay time was chosen optimally in a compromise between the largest dynamic range of velocity and acceptable loss of correlation due to out-of-plane motion. The measurements were done at a recording rate of 20 Hz for the duration of 79 s in order to obtain statically independent samples of turbulent suspension flow in 1578 PIV images.

3. Flow condition

One useful aspect of this flow apparatus is that the flow is driven by gravity alone. By balancing all forces acting upon an element of flow and with the assumption of not being any acceleration in flow, the wall shear stress can be obtained as the following where θ is the angle of the water table with respect to the horizon, h is the thickness of film flowing and ρ is the density of fluid, as shown in Figure 46.

$$\tau_w = \rho g h \sin\theta$$

So:

$$u_\tau = \sqrt{\tau_w/\rho} = \sqrt{gh\sin\theta}$$

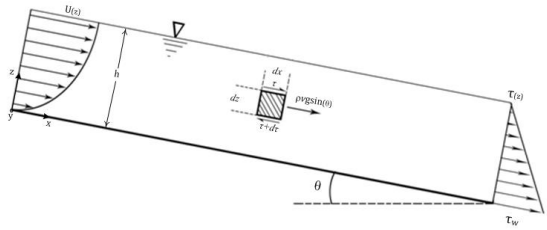

Figure 46 The film flow falling on inclined plate;

The friction Reynolds number is in turn obtained based on the thickness of h and the friction velocity $\mathbf{u_\tau}$ as:

$$Re_\tau = \frac{h.u_\tau}{\nu} = \frac{h.\sqrt{gh\sin\theta}}{\nu}$$

Where ν is the kinematic viscosity of fluid and g is gravity acceleration. It is notable that the considered flow on the water table can be approximately characterized as a half channel flow and Re_τ (based on the film thickness, which corresponds to the channel half-width in the channel flow study) can be determined directly from geometry and fluid properties.

Velocity profiles of the single-phase flow measured by Laser Doppler Velocimetry (LDV) at the acquisition points around the field of view in upstream, downstream, and two spanwise positions have showed excellent agreement with DNS data for a fully developed turbulent channel flow. For more details, the reader is referred to M. Kvick [69] where the same setup was used.

3.1. Evaluation of flow quality

Before performing the main experiments with fiber suspension, a series of PIV measurement on pure flow was done. PIV processing procedure will be described in the next chapter. To examine the quality of the flow within the measurement area on the water table, the experimental data obtained were compared with DNS results for fully developed turbulent channel flow. For all cases of the experiment, the thickness of film flow was set on 11.5±0.5 mm by controlling the flow rate of the pump for the table angle of 0.081±0.005 deg for Re_τ=150. In this configuration, we could establish a no acceleration condition for the flow over the test section.

One of the controversial questions in most of the channel or open channel flow studies is determination of the location where the fully developed turbulence regime is occurred. Typically, in this type of studies the definition of the entrance length is used to refer to the distance where beyond that the fully developed turbulence is dominant. This subject has been investigated in several studies, Dean [70] and Zanoun [71]. However, there are no common consensuses on a certain range for this parameter. Nevertheless, to verify the fully developed turbulent flow in the experiment domain, two PIV measurements were done with and without the tripping wire at the entrance of the flow into the test section while water table was set for the friction Reynolds number of 150.

Furthermore, we assessed the turbulence homogeneity. The measurement area was divided into two different sub-areas in streamwise, and three different sub-areas in spanwise direction, as shown in Figure 47, and the flow over these areas was independently measured for Re_τ=150. There was a good homogeneity in spanwise and streamwise direction. The deviation of the data was less than 1.1%, and the reason for this can be due to the not re-aligning the laser sheet respect to the wall when it was shifted to the upstream position.

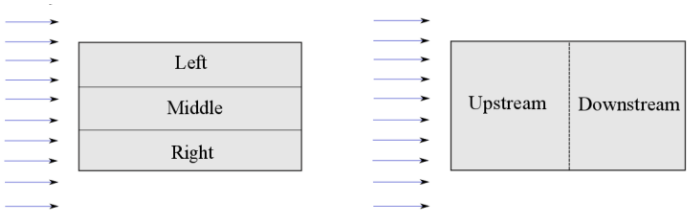

Figure 47 Homogeneity assessment;

Finally, in order to check the repeatability of the experiments with different parametric values, while Re_τ is fixed, an additional series of tests were carried out. In these test cases, the water table inclination angle was changed, and correspondingly the film thickness was altered to keep the Re_τ constant at 150.

The results of the velocity profile and root mean square (*rms*) values of streamwise velocity for all test cases above are presented in Figure 48, where the comparison between DNS data of fully developed turbulent channel flow, Kawamura Lab [72], and experimental data obtained shows a strong agreement. Uncertainties in the bulk velocity and velocity *rms* value were less than 5% at 95% confidence level. This demonstrated that the flow is fully developed turbulent over the slightly inclined table and that it compares well with DNS database of turbulent channel flow. Any minor deviations, however, can be due to probable human errors related to the experimental setup and limitations of the measurement technique, especially for the data points very close to the wall.

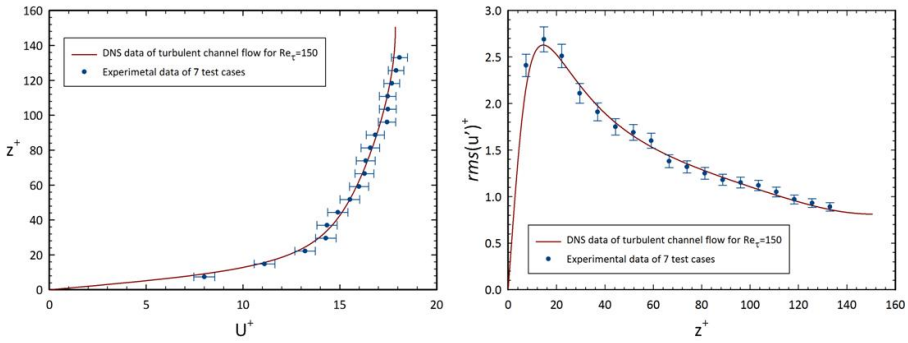

Figure 48 Velocity profile and streamwise velocity rms for Reτ=150; (•) experimental data for 7 independent test cases; (-) DNS database for fully developed turbulent channel flow of Kawamura lab; dimensionless based on wall variables;

Figure 49 shows a sample of the vector field and vorticity field measured at the plane of z^+=14. The low-speed and high-speed streaks of the flow with the clearance of $\lambda^+ \approx 100$ are observable. These near-wall coherent structures of turbulent flow are well known.

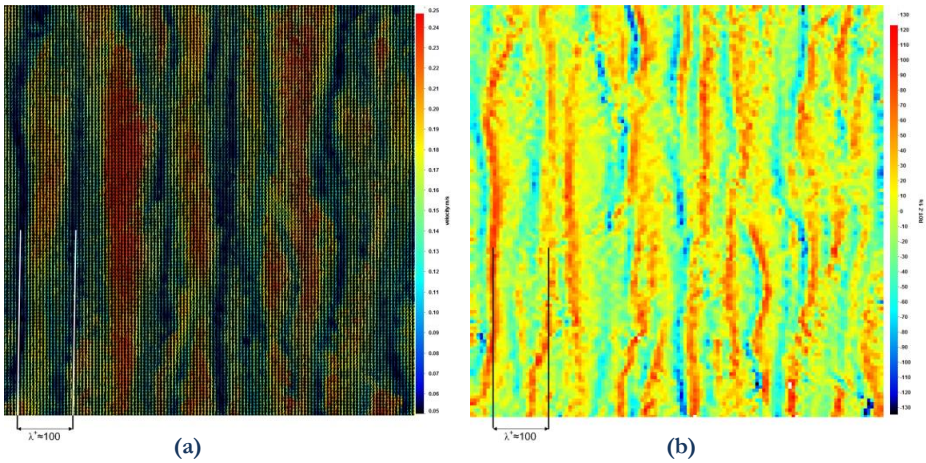

Figure 49 (a) velocity field; **(b)** vorticity field (ω_z) at z^+=14;

4. Suspension experiments

We used dilute suspensions (volume fraction $\Phi_v \approx 2\times10^{-5}$) of cellulose acetate fibers with density of 1300 kg/m3 and diameter of 70 μm in tap water. The experiments were conducted for three different types of fibers in length: 0.5 mm, 1mm & 2 mm corresponding to aspect ratios of 7, 14 & 28 respectively. For all cases, the fiber concentration in the measurement volume, nl^3 where n is the number density of fiber and l is the fiber length, was less than 10^{-2}. This suggests the interaction between the fibers and the fiber effect on flow rheology will be weak [73].

The measurements were carried out in three levels approximately z^+=14, 43 & 72 (in wall unit) from the bottom wall. These three levels were chosen based on the fact that these levels cover the plenty of the information of flow turbulence mechanism, and the fibers have the most fluctuations in these regions due to the surrounding fluid fluctuations. In addition, the preferential concentration of fibers likely takes place near the wall. The matrix of experiments is presented in Table 3. All experiments were set for Re_τ=170.

The fiber Stokes number is other key parameter, defined as the ratio between the fiber relaxation time and flow characteristic time, $St=\tau^+=\tau_{fib}/\tau_{flow}$. The Stokes number shows the relative influence of the fiber inertia, i.e. how fibers move independently of the turbulent eddies. The flow time scale used widely in numerical works is taken as $\tau_{flow}=\nu/u_\tau^2$ presenting the viscous time scale of the flow, which is the time available for eddy-particle interaction. However, we believe that the fiber response time scaled on Kolmogorov time scale demonstrates fiber dynamics more

adequately because fibers are under the influence of local structures of flow that Kolmogorov scales represents them. The dynamic response of non-spherical particles is orientation dependent. Shapiro and Goldenberg [17] proposed an equivalent response time for fibers based on the assumption of isotropic particle orientation and the orientation averaged resistance: $\tau^+ = \frac{2}{9} \frac{S a^{+2}}{\lambda} \frac{\lambda \ln(\lambda+\sqrt{\lambda^2-1})}{\sqrt{\lambda^2-1}}$, where S is the ratio of the fiber density to fluid and a^+ is dimensionless semi-minor axis of fiber with aspect ratio of λ. The fiber specifications are also summarized in Table 3.

Table 3 The fiber specification and the matrix of experiments

	Fiber specification			Measurement position		
	length (mm)	aspect ratio (λ)	response time (τ^+)	Z^+=14	Z^+=43	Z^+=72
Case 1	0.5	7	0.2	√	√	√
Case 2	1.0	14	0.24	√	√	√
Case 3	2.0	28	0.3	√	√	√

As a reference for the fiber suspension measurements, before introducing fibers into the flow, the pure flow in the test section was first assessed in the levels specified. This was done using the same setup as it would be used for the suspension flow experiments in order to ensure that any observed changes in flow statistics cannot be caused by the measurement setup.

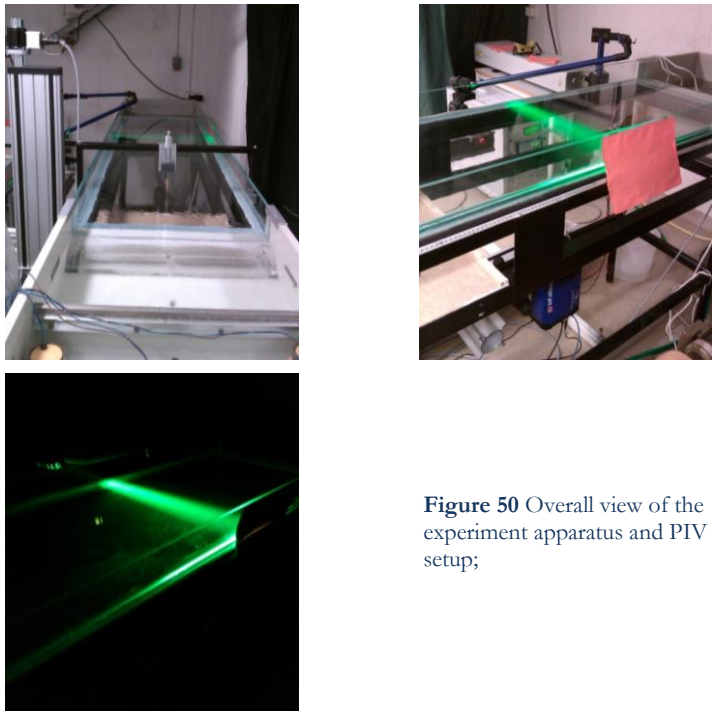

Figure 50 Overall view of the experiment apparatus and PIV setup;

Chapter 5

PIV/PTV Image Processing Procedure

Applying the PIV/PVT techniques to dispersed multiphase flows introduces problems related to discriminating between the tracers representing the fluid phase flow and the suspended particles or fibers. In order to obtain accurate carrier phase velocity fields of suspension, the particle or fiber images must be eliminated from original images prior to PIV data processing. The PTV data processing must be only applied to the images of fibers as well.

1. Phases separation

Because of the optical measurement setup, we employed the spatial median filtering proposed by Kiger & Pan [60]. This technique utilizes the size difference between the tracer particles and suspended objects. It can be applied to solid-liquid two-phase turbulent flows to provide a reliable technique for phase separation in single-camera images. The performance of the separation process depends on the filter size and the ratio of suspended object and tracer image size.

The procedure for the cases is illustrated in the sample images in Figures 51 (a-c). The small tracer particles with size of 2 pixels can be removed by applying a 5×5 window of local median filter to the raw image, a sample of raw images in Figure 51(a). The value of each pixel is replaced with the median value of its neighbors in window. The result is the image of fibers with a mean diameter of 6 pixels, Figure 51(b). Subtracting the resulting image from the original one leaves only the tracers in image acceptable for PIV processing, Figure 51(c). Therefore, the fiber and fluid-phase velocity can be calculated using Fiber Tracking Velocimetry and PIV technique, respectively.

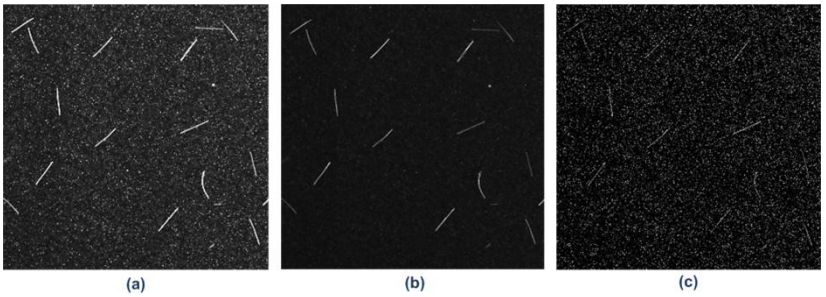

Figure 51 Example of sequence of image pre-processing procedure; **(a)** original two-phase image including tracers and fibers; **(b)** fibers image obtained with the filter width 5×5; **(c)** fluid phase image resulting with just traces;

Filtering with the median filter will influence the accuracy of the displacement calculation through residual images of fibers left by the image separation process, Figure 51(c). This results from erosion of fibers by the filter, and hence an incomplete removal when it is subtracted from the original image. Kiger & Pan showed that a filter with width of $f/dt>2.0$, where f and dt are the filter size and tracer size in an image, will provide average displacement errors in the tracer flow field in the order of 0.02 pixels. In addition, the images can be improved by some image pre-processing techniques to reduce errors, described in the next section. Here, the median filter size of 5×5 was chosen after a trial and error procedure, when the fluid velocity field showed a satisfactory signal to noise ratio. Typically, the peak-to-peak ratio in the correlation map exceeded 2.7 and more than 97% of vectors were extracted as correct vector.

2. PIV image processing

PIV data processing was performed by DaVis 7.2 for both the clean flow (single phase flow) and the fluid phase of the fiber suspension flow. The PIV images were preprocessed to improve the quality of the results. Using sliding background filtering in size 7 pixels, we subtracted the large intensity fluctuations in the background due to reflections etc. We also normalized particle intensity in images. This option applies a local particle intensity correction using a MIN-MAX filter. As a result, we obtained homogeneous particle intensities so that small particles could also contribute to the correlation.

The vector field computation was carried out using a three-pass cross-correlation algorithm (FFT-based) with decreasing interrogation window size from 64×64 to the final size 32 × 32 pixel interrogation windows with 50% overlap. This resulted in an array of 126×126 vectors with a final vector spacing of 0.5 mm. The multi-pass with decreasing window size helps to correlate the correct particles and

improves the signal-to-noise, thus enhances the spatial resolution of the vector field and produces less erroneous vectors.

Once the vector field has been calculated, vector validation algorithms were applied to eliminate spurious vectors. The information obtained from the scatter plot of displacements was useful to select an allowed vector range that restricts the filtered vectors. Any vector outside this range was removed. In addition, the first to the second peak ratio factor of two in the cross-correlation map was used as a post-processing criterion for eliminating questionable vectors below this threshold. In general, higher peak ratio factor indicates more confidence in the vector.

Furthermore, In order to find and remove erroneous vectors with more efficiency, a local median filter was applied in post-interrogation procedure. The local median filter computes a median vector from the neighbor vectors and compares the center vector with *this median vector* ± *an allowed deviation*. The center vector is regarded as a spurious vector and removed from the vector field when it is outside this allowed range. This way is a reliable method for identifying and removing spurious vectors even when many spurious vectors are present, Westerweel [36]. The deviation of "*1.5×rms of neighbor vectors*" was chosen in a trial and error procedure depending on the turbulence of the vector field processed.

3. Fiber Tracking Velocimetry

Fiber Tracking Velocimetry is the estimation of velocities of individual fibers tracked in consecutive images deriving their trajectories in visualizations of suspension flow. The fiber tracking itself consists of two fundamental parts, *i)* identifying fibers in visualization volume, and *ii)* matching pair those in consecutive images.

3.1. Fiber identification

In order to determine the position and orientation of fibers in images, an image-processing algorithm in the class of steerable filters implemented in MATLAB was used. This type of image filters for ridge detection has been proposed by Jacob and Unser[74] and has been developed and evaluated by Carlsson et al [62] for fiber detection. The ability of this filter for identifying fibers in digital images obtained from visualization of flowing suspensions has been found to be excellent with acceptable accuracy. In the procedure of fiber recognition, we need a threshold on brightness level of fibers to recognize reliably those that are in the light sheet (measurement volume). A dynamic threshold described in the next sections is introduced for this purpose.

-Light scattering from cylindrical fiber in oblique incidence

In this part, we explain the dependence of light scattering from a finite fiber on the incidence angle of the light beam and the fiber. A discussion of solutions to some of the problems involving light scattering from arbitrarily oriented infinite or finite cylinders already studied will be found in the literatures[75-78]. It is quite probable that the mathematics developed so far will not be capable to explain the light-scattering patterns from finite fibers in PIV measurement of suspension, i.e. something like Mie theory for light scattering from tracer spheres. Even so, existing treatments are useful here because they explain the unique type of light-scattering pattern produced by fibers like optically ideal cylinders, and this should be understood by anyone involved in optical diagnostics of the fiber suspension flow.

When a narrow beam of monochromatic parallel rays from a laser collides with a straight translucent fiber in an angle of incidence, the rays will be diffracted, reflected, refracted, and omnidirectionally scattered. The omnidirectional scattering of light is caused by optical imperfections. Cohen and Acquista [77] found an equation for the intensity of the scattering of a ray that hits obliquely on the surface of an extremely long taut fiber that is assumed optically ideal, i.e. it has a smooth external cylindrical surface, a circular cross-section, translucent, and optically homogeneous and isotropic. It can be predicted that the scattered radiant energy, mostly including reflected, and refracted lights, emerges along the surface of the cone whose half-apex angle is the angle between the cylinder axis and the direction of the incident beam and is viewed on a circle, sighting towards the apex of the cone. The geometry of characteristics of light scattered by a tilted infinite cylinder in light sheet is shown in Figure 52(a).

The diffraction of the light consists of a series of spots generated by the constructive and destructive interference of the rays transmitted by the fiber and those are bent into the shadow of the obstacle when encounter the edges, and depends on the ratio of obstacle diameter and wavelength. At oblique incidence, these spots appear only on the surface of this cone, and its intensity decreases as inverse ratio of distance from the cylinder.

At lower aspect ratios, the characteristics of the scattering begin to exhibit finite-size effects. The scattering pattern becomes diffused, with the large deviation from scattering along the cone surface occurring for infinite cylinders. While aspect ratio is decreasing, the scattered light energy distribution is beginning to approach a Mie scattering pattern, but the effects of the cone representing scattering pattern along are still clear in a slightly skewed distribution.

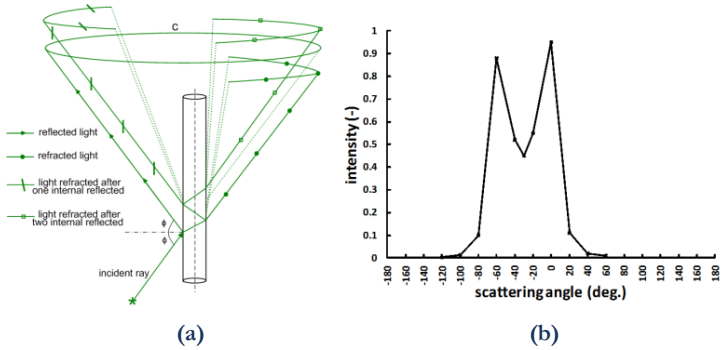

Figure 52 (a) the geometry light scattering from an infinite cylinder in an incidence angle [78];
(b) the intensity of light scattered by a cylinder with aspect ratio 20 in the incidence angle of 60°[77];

As a special case, the intensity distribution of scattered light for a cylinder with aspect ratio of 20 in the incidence angle of 60° is shown in Figure 52(b) from reference [77]. The two peaks representing scattering along the cone surface are still clearly distinguishable, but the distribution is much diffused.

-Light scattering from the finite acetate cellulose fibers in visualization

The specifications of the experiments that influence optical measurements of fiber motion comprise colorless acetate cellulose fibers with a diameter of 70 μm and aspect ratio of 7, 14 & 28 and refractive index n=1.5. The laser beam has a wavelength of 527 nm. The CMOS chip of the camera as light detector is in a perpendicular position to the incidence plane of the light and fiber, in 2D view. The fiber diameter is comparably bigger than light beam wavelength, thus diffraction effects are negligible.

Figures 53(a-c) depict the dependence of the brightness level (normalized with the maximum value in each case) of fibers in images on incidence angles of the laser beam in the suspension visualization. The incidence angles are measured relative to the perpendicular to the axis of the fiber as the ϕ=0 means normal incidence and ϕ=90° (or -90°) means that the laser beam and fiber are at the same direction. As seen in Figures 53, at the region of normal incidence, the light intensity of fibers are dispersed in a wide range from max 1 to minimum about 0.03. The dense region of intensity dispersion of fibers move to lower intensities when the light direction incline away from the normal incidence to ϕ= 90° (or -90°) where laser beam and fiber are parallel. At ϕ= 90° (or -90°), this region is remarkably thin and almost there are no intensity zones with high density.

As mentioned in the previous part, for aspect ratios in order of 20, light scattering is along a diffused cone with half angle of 90°-ϕ, although there is some

omnidirectional scattering caused by optical imperfections. Therefore, at ϕ=90° (or -90°) there is no cone surface that concentrated energy of scattered light propagates along that and there are just scattering due to optical imperfections of fibers. If we assume a 2D orientation in parallel sheets, and only a small fraction of fibers is in light sheet and the rest is in the expansion of the laser sheet, we can conclude that almost all fibers recorded in the range of incidence angle of 90° are in light sheet. In the light sheet, the power of illuminating laser is strong enough that omnidirectional scattering of light from these fibers can charge the camera chip to record. On the other hand, all fibers that are in normal incidence of the light beam scattered a wide range of intensities according to their distance to center of light sheet so that those that are in light sheet have high intensity. When fiber aspect ratio decreases, the evidence of cone of light scattering is spread out more. Consequently, it is predictable that dependence of their brightness on incidence angle decreases, although this dependency exist yet. This is observable on Figure 53 for the fibers of λ=14 &7.

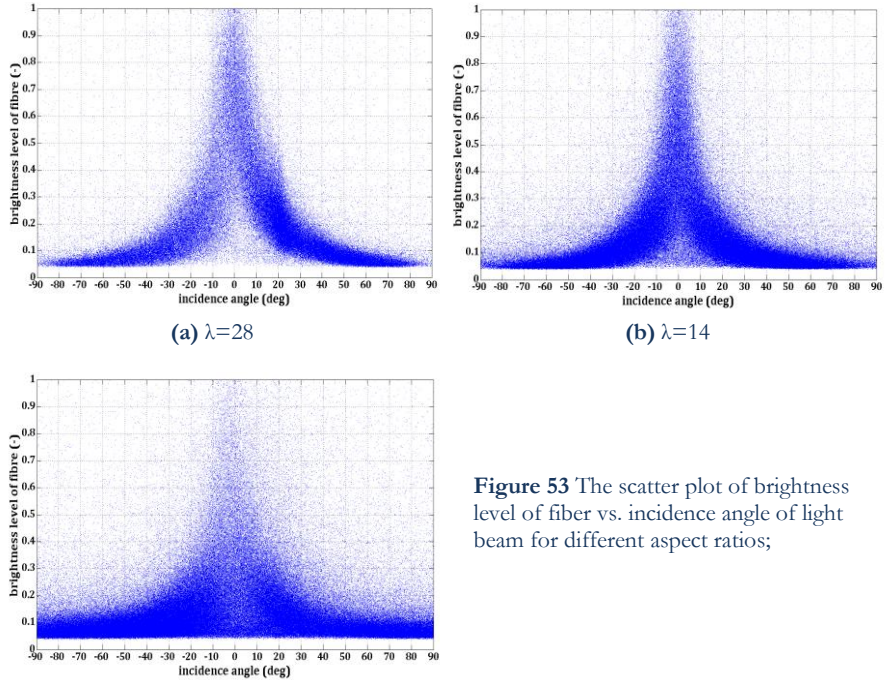

(a) λ=28 **(b)** λ=14

(c) λ=7

Figure 53 The scatter plot of brightness level of fiber vs. incidence angle of light beam for different aspect ratios;

We can reach briefly the following two principals:

1- Of the fibers that are at the same direction, those that have the highest brightness are in the light sheet.

2- For the fibers that are in light sheet, the more inclined to the normal direction to the light beam, the higher intensity of light scattered.

This dependence of fiber brightness on light incidence angle leads to that the brightness of fiber images quite varies with respect to their direction to the light beam as well, not only because of being out of light sheet. The dependence of fiber brightness on the light direction can be seen in Figure 54.

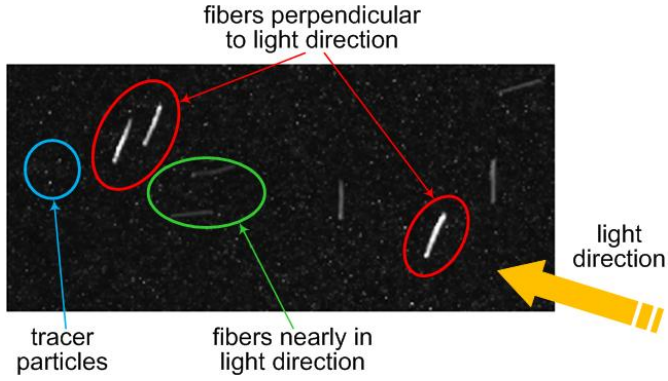

Figure 54 A sample image of fibers brightness in PIV measurement;

-Dynamic threshold to recognize fibers in visualization volume

The dependence of intensity of light scattered by fibers on their orientation relative to the light beam direction causes that we cannot simply discriminate between the fibers in the light sheet and those are outside using just the fiber brightness in images. It was found that two fibers at the same level in light sheet, but with two different orientations will have different brightness in images, the one closer to the normal direction to the light beam is brighter, and the one that is more aligned in light direction appears darker. In addition, at the same angle the fibers that are in the light sheet will be highly brighter in comparison with the other fibers outside, in the expansion region of the light sheet. Nevertheless, this problem does not seem to have attracted much consideration from researchers working on fiber tracking. The common method of individual particle detection has been single threshold binarization. This single threshold level in most PIV/PTV recordings will result in either capture of a large number of fibers out of light sheet or a considerable loss of the fiber data. Therefore, to reach a confident method, if we choose the relevant level of brightness as a threshold for any range of fiber angle to

set as threshold instead of a fixed constant threshold overall orientation, we will be able to identify fibers that are in the light sheet properly. Thus, we will have different threshold for different orientations.

The basic concept of the dynamic threshold is to adjust a brightness level for each range of fiber orientation according to being of fibers in light sheet with a specified confidence level. This concept is illustrated through Figure 55 (a-c). The histogram of mean brightness level of fibers for a selected range of fiber orientations (70° to 80°) and the case of fiber λ=14 at z^{+}=43 is presented in Figure 55(a). This distribution has a skewed shape, and we found the Generalized Extreme Value Distribution (GEV) could well model both high peak and long tail of the distributions in a fitting manner, red curves in Figure 55(a). Now if we put the purpose on finding fibers in light sheet with a confidence level 95%, we must determine a brightness level that the probability of the being of fibers is 95%, thus the fibers having higher brightness than that threshold are the relevant fibers for us, i.e. they are in the light sheet. The Cumulative Distribution Function of these distributions gives us the threshold on the brightness that the values greater or equal will have the probability 95%, Figure 55(b). The thresholds to identify fibers in the light sheet with 95% confidence have showed on Figure 55(c).

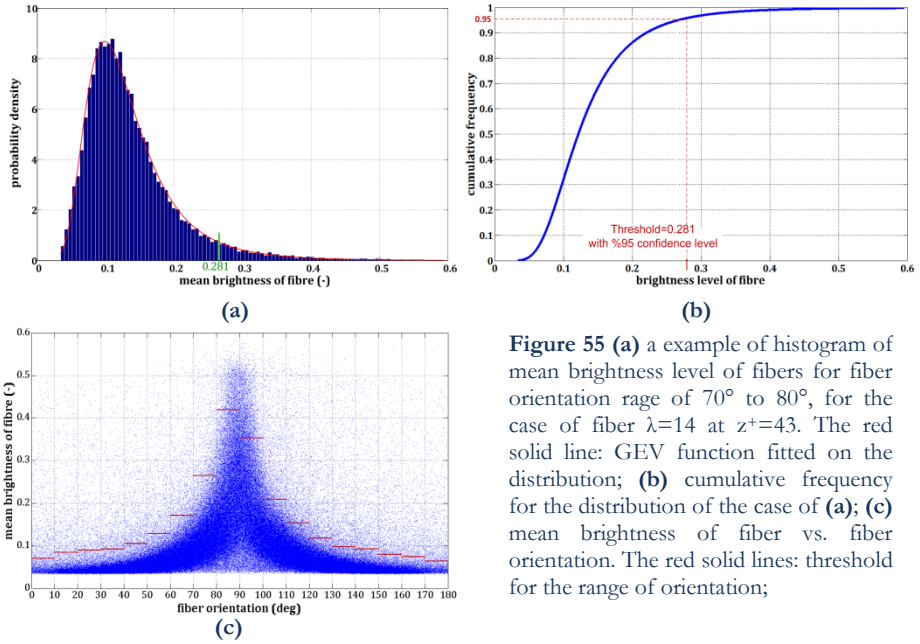

Figure 55 (a) a example of histogram of mean brightness level of fibers for fiber orientation rage of 70° to 80°, for the case of fiber λ=14 at z^{+}=43. The red solid line: GEV function fitted on the distribution; **(b)** cumulative frequency for the distribution of the case of **(a)**; **(c)** mean brightness of fiber vs. fiber orientation. The red solid lines: threshold for the range of orientation;

3.2. Fibers pair matching

After detecting fiber position and orientation reliably in visualization volume, we need to match the corresponding ones in sequential images to estimate their displacement and accordingly their velocity.

Because the orientation of fibers has a significant role in pairing as well as their position, in case of tracking fibers in suspension flows, it was used the matching algorithm based on SOM neural network in order to meet the requirements for more reliable matching at larger numbers of dispersed fibers and more robustness against loss-of-pair fibers between successive frames. This algorithm and its capability of tracking were discussed in detail in chapter 3.

"It doesn't matter how beautiful your theory is, it doesn't matter how smart you are. If it doesn't agree with experiment, it's wrong."

Richard Feynman

Chapter 6

RESULT AND DISCUSSION

The current work focuses on the statistical characterization of the rod-like stiff fiber motion in wall-bounded turbulent flow. The fiber distribution, orientation and velocity statistics for three different aspect ratios (λ=7, 14, 28) and at three different wall-normal distances (z^+=14, 43, 72) are reported and discussed. The objective is to study the effect of aspect ratio, accordingly fiber length (size effect), and local flow structures on the behavior of long fibers (longer than local flow scales) in a wall turbulence. In addition, the total orientation distributions of fibers in measurement volume are present.

Figure 56 shows the polar histogram of the fiber orientation in the visualization volume including the fibers creeping on the wall. It illustrates that orientation distribution of fibers depends considerably on fiber length. The short fibers (λ=7) are distributed mostly in orientations of 0°- 45° and 135°- 180° where angle of 90° is in mean flow direction. The fibers with moderate size (λ=14) have a nearly isotropic distribution. Long fibers (λ=28) are orientated significantly in the main flow direction. It can be due to the competing effects of the sedimentation and the wall contact versus fluid inertia for different sizes of fiber, where the sedimentation and direct wall contacts drive the orientation towards the spanwise direction and the fluid inertia tends to drive the fiber orientation towards the flow direction.

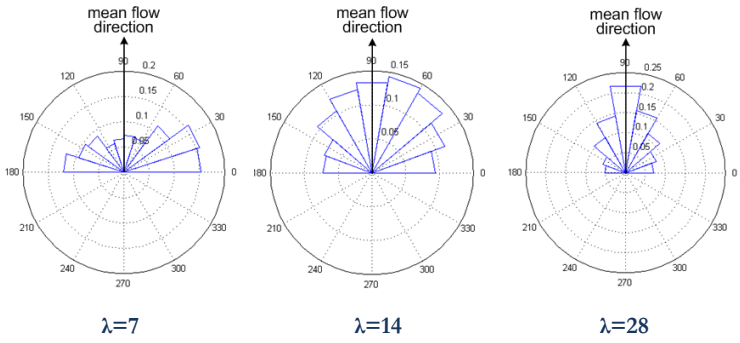

Figure 56 The polar histogram of fibres orientation;

The velocity statistics of the fibers and the surrounding fluid is summarized in Table 4(a-c). In order to quantitatively express the fiber fidelity in following the

fluid motion only by a single value, the correlation coefficient for the fluctuating velocity of fiber and surrounding fluid are presented, see Table 4. The fiber-fluid fluctuating velocity correlaton is defined as the correlation between the fiber and fluid fluctuating velocity measured at the same point in the space and time. This correlation coefficient provides the strength of particle-fluid interaction. To do this, after determining of the position of fiber velocity vector from the fiber tracking at the center of the fiber, the fluid velocity data in the neighborhood of fiber are extracted from a search area around the fiber center, which its size is twice the interrogation window size used in PIV calculation. The fluid velocity at the position of the fiber center is interpolated as a representative of the surrounding fluid velocity. The mean and fluctuating velocities are defined as follow (the same definition for streamwise velocity (U) and spanwise velocity (V)):

$$U_{fiber} = \overline{U}_{fiber} + u'_{fiber} \qquad \text{and} \qquad U_{fluid} = \overline{U}_{fluid} + u'_{fluid}$$

The root mean square (*rms*) of the velocities is calculated as:

$$rms(U_*) = \sqrt{\frac{\sum_{i=1}^{N} u'^2_{*i}}{N-1}}$$

Where * denotes fiber or fluid, and N is the total number of the extracted fiber or fluid velocity. The correlation coefficient is an indicator to the level of dependency of two random variables (u'_{fiber}, u'_{fluid}). There are several ways to indicating the degree of dependency for two random variables. The Pearson correlation coefficient is the common way to define a measure of the linear relationship between two variables [79].

$$R\left(u'_{fiber}, u'_{fluid}\right) = \frac{1}{rms(U_{fiber}) \times rms(U_{fluid})} \times \frac{\sum_{i=1}^{N} u'_{i\,fiber} \times u'_{i\,fluid}}{N-1}$$

When the fiber velocity is different from the surrounding fluid velocity because of fiber inertia, gravity or moving through different flow regions, the fiber relative velocity, referred to as fluid velocity seen by fiber, is a significant variable. The fiber relative velocity is defined as: $\Delta U = U_{fluid} - U_{fiber}$.

Table 4(a) The velocity statistics of fiber and the surrounding fluid velocity for case1: λ=7, τ^+ = 0.2

z^+	$\overline{\Delta U^+}$	$rms(\Delta U^+)$	$\overline{U}^+_{fiber}$	$\overline{U}^+_{fluid}$	$rms(U^+_{fiber})$	$rms(U^+_{fluid})$	$R(u^{+}_{fiber}, u^{+}_{fluid})$	$R(v^{+}_{fiber}, v^{+}_{fluid})$
14	2.79	3.84	9.83	12.62	3.94	2.51	0.36	0.15
43	0.53	2.40	14.32	14.86	2.59	1.76	0.44	0.36
72	0.47	1.71	15.70	16.17	1.94	1.46	0.53	0.41

Table 4(b) The velocity statistics of fiber and the surrounding fluid velocity for case1: λ=14, τ^+ = 0.24

z^+	$\overline{\Delta U^+}$	$rms(\Delta U^+)$	$\overline{U}^+_{fiber}$	$\overline{U}^+_{fluid}$	$rms(U^+_{fiber})$	$rms(U^+_{fluid})$	$R(u'^+_{fiber}, u'^+_{fluid})$	$R(v'^+_{fiber}, v'^+_{fluid})$
14	0.71	3.30	11.77	12.48	3.70	2.51	0.44	0.24
43	0.65	2.32	14.34	14.99	2.49	1.70	0.49	0.35
72	0.53	1.74	15.70	16.25	1.98	1.47	0.52	0.40

Table 4(c) The velocity statistics of fiber and the surrounding fluid velocity for case1: λ=28, τ^+ = 0.3

z^+	$\overline{\Delta U^+}$	$rms(\Delta U^+)$	$\overline{U}^+_{fiber}$	$\overline{U}^+_{fluid}$	$rms(U^+_{fiber})$	$rms(U^+_{fluid})$	$R(u'^+_{fiber}, u'^+_{fluid})$	$R(v'^+_{fiber}, v'^+_{fluid})$
14	-0.68	3.73	11.65	10.97	4.17	2.87	0.48	0.24
43	-0.28	2.25	14.84	14.57	2.44	1.90	0.49	0.33
72	0.44	1.58	15.71	16.14	1.90	1.39	0.57	0.44

As seen, the correlation coefficients for all cases increase with an increase in the wall-normal distance. It can be concluded that fibers in the regions far away from the wall follow the fluctuations of fluid better than the ones are near the wall. The reason can be that fluid fluctuations are the highest near the wall so that the fiber inertia does not allow fiber to pursue the fluctuations completely. On the other hand, the degree of following the fluid motion for long fibers (λ=28) in the near-wall areas is higher than the short fibers (λ=7). It can be due to the fiber length. It is notable that the fiber time response is in the order of one for all cases. Although long fibers show a considerable level of correlation with fluid fluctuations near the wall, negative mean relative streamwise velocity is observed for them. However, these negative quantities are not in high order.

In Figures 57, the distributions of fiber streamwise velocity for the three aspect ratios and the three levels are depicted together with the corresponding fluid velocity. It can be observed that for the case of fibers with aspect ratio 28 at the region near the wall, z^+=14 where the flow fluctuations are the most extensive, the fiber velocity distribution exhibits two distinct peaks in two different zones (zone *I* and *II*). The zone *I* accords with the position of low-speed streaks of flow, and the zone *II* corresponds with the position of high-speed streaks. The fibers belong to zone *I* have the velocity less than mean fiber velocity and are in low speed area of flow, thus these fibers have come from lower layers with lower momentum to this layer. On the other hand, the fibers in zone *II* have a velocity higher than the mean velocity of fiber in this level coming from upper layers with higher momentum. Moreover, the mean velocity of fibers almost conforms to flow mean velocity. Although we have not measured wall-normal velocities, it can be hypothesized that the zones of *I* and *II* are respectively associated with the ejection and sweep environments known in wall turbulence mechanism. Decreasing aspect ratio, and

accordingly decreasing fiber length, the evidence of these zones and peaks is disappearing. For the case of fibers with aspect ratio 7, the fibers mean velocity obey the dominant flow velocity in low-speed streaks. In higher levels, the fibers mostly follow the dominant local flow regardless their size.

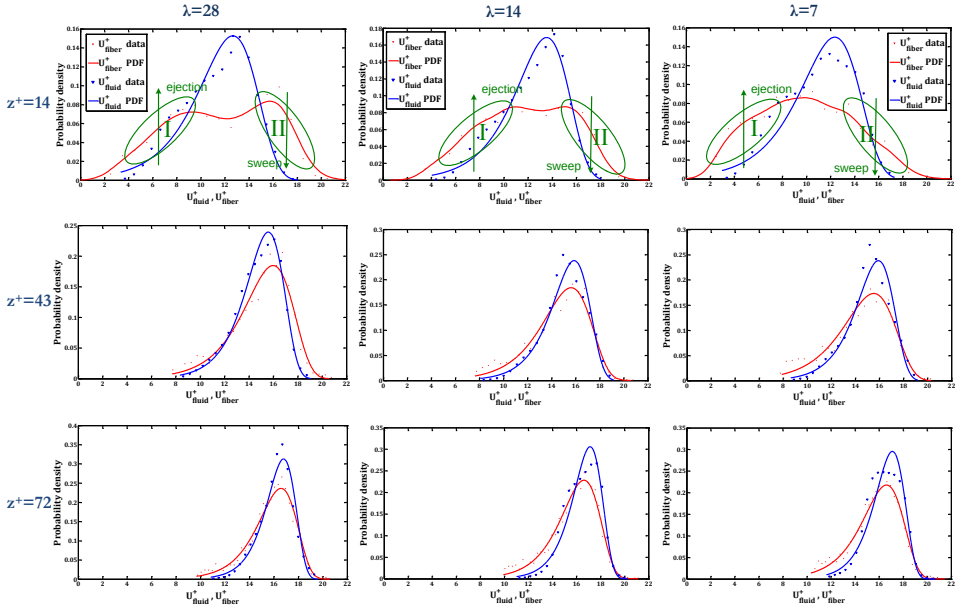

Figure 57 The fluid and fiber streamwise velocity distribution for three different aspect ratios and in three different wall-normal distances;

Figure 58 shows the distributions of fiber streamwise velocity assembled for all cases. As seen, the fiber translational motion is practically unaffected by the aspect ratio, whereas it depends crucially on local flow structure in different layers. This has been already observed for the ellipsoidal particles in DNS results [29]. In the region near the wall (z^+=14), the distributions of fibers streamwise velocity cover a wide range of velocities due to existing wide range of turbulence scales near the solid wall. However, different trends are observed for fibers with different size. In upper layers, the fiber aspect ratio (fiber length) considerably loses its significance. This shows that the fiber length has a key role in the fiber behavior in the regions near the wall.

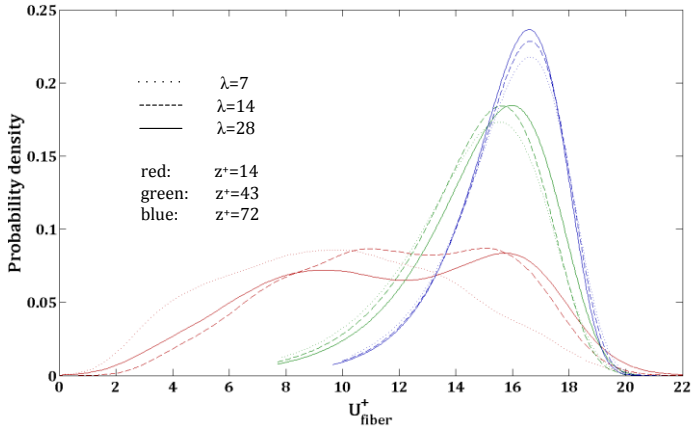

Figure 58 The superimposed fiber velocity distributions for three different aspect ratios and in three different wall-normal distances z^+=14, 43 72;

Such observations can be explained by looking at fiber rotation. The fibers tend to rotate about the spanwise axis (y-axis) due to the streamwise mean shear field [21]. In the far field, where the distance from the wall is greater than the fiber length so that the fiber can rotate freely, the fiber motion can be perfectly described by Jeffery's equations [80]. Therefore, the experimental results confirm previous numerical results. For distances fewer than the fiber length, the fibers experience a fiber-wall interaction, and the wall ceases fiber rotation. This causes that the fiber offends Jeffery's manner. This is why the experimental observations do not agree with the numerical results for the near-wall regions.

The orientation of fibers does matter since it influences the fiber dynamics. In addition, it has practical importance in the quality of production in papermaking industries [2]. It has been observed numerically by Zhang et al. [21] and Mortensen et al [29] that small ellipsoidal particles have preferential orientation in streamwise direction. Newsom and Bruce [19] found that the orientation preference was more sensitive to fiber diameter than to length. The fibers with larger diameter displayed a greater tendency for horizontal orientation during their experiments about horizontal orientation properties of fibrous aerosols in atmospheric turbulence.

The scatter of the fiber streamwise velocity versus fiber orientation is exhibited in Figure 59 for the near-wall level. The angle that describes the fiber orientation is defined relative to the mean flow direction as the $cos(\theta)$=1 means the fiber oriented in the streamwise direction. In Figure 59(a), high concentration of long fibers in two zones, zones *I* and *II*, is clear. It exhibits a high tendency of low speed fibers to orientate in streamwise direction, zone *I*. On the other side, the fast long fibers do not have a preferential orientation and are distributed in every direction, zone *II*.

These two zones can be corresponded to two events of ejection and sweep mentioned previously. The fast fibers are in sweep environment in the upper layer and under the influence of extensive fluctuations surrounding. The low speed fibers are in low sweep areas in the vicinity of the wall, and the wall has a stabilizing effect on them.

Decreasing fiber length broadens the zone *II* so that there is no evidence of preferential velocity or orientation in this zone for the short fibers, Figure 59(c). However, the short fibers are still oriented mostly in streamwise direction for a certain range of velocity, zone *I*.

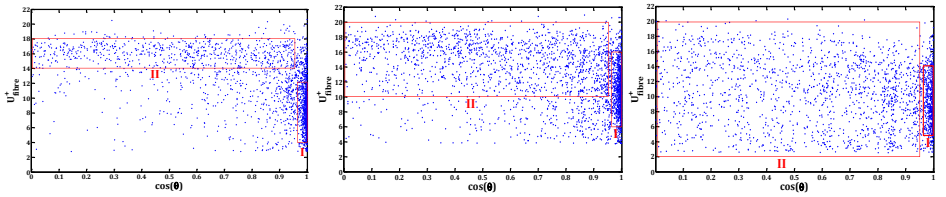

(a) λ=28 (b) λ=14 (c) λ=7

Figure 59 The scatter plot of the fiber streamwise velocity versus fiber orientation, z^{+}=14;

My purpose is to describe a mechanism for these fiber behaviors observed. To this, I have to join all the phenomena already observed. It has been apparent that the strong sweeps and ejections carry particles toward and away from the wall, conditioned by the presence of particles to be transferred. It leads to preferential distribution. These coherent events are generated by the near-wall coherent quasi-stream wise vortices [7-9]. These quasi-stream wise vortices are parallel counter-rotating vortices, which lay and bound the low-speed streak as arranged in a series of alternating intervals. The ejection events on the upwash side contribute to lift low-speed streaks. However, in most of cases, these clockwise and counterclockwise quasi-streamwise vortices are not paired in equal size and strength. Each mature quasi-stream wise vortex often follows a small quasi-stream wise vortex of opposite sign, offspring vortex, interpreted as the rear, wall-touching end of a counter-rotating quasi-streamwise vortex farther downstream, in a turbulence regeneration cycle. Marchioli and Soldati [81] showed the role of the offspring vortex in trapping the particles in the wall layer.

Here, the evidences are presented that the probability of existing high aspect ratio, here let us give it a physical sense and say long fibers, in sweep and ejection environments is higher than being trapped in certain areas. It can be explained that long fiber in the outer flow is captured by a sweep. It approaches the wall and moves between the vortex and the wall. The fiber may touch the wall surface or not. Afterwards, the fiber on the upwash side of the vortex is subject to the

influence of the ejection. Since the long fibers reacts to flow fluctuations as fast as possible due to the increase in the efficiency of the interception mechanism of long fibers by the wall, the longer fibers experience a short residence time into low-speed streaks. It can cause a nearly equal rate of fiber transfer toward and away from the wall in sweep and ejection events. Nevertheless, it has been numerically observed for point-mass ellipsoidal particles that there is a net transfer of fibers towards the wall and the fibers remain trapped for a long time into the low-speed streaks where the flow fluctuations are not strong enough. On the other hand, the probability of being short fibers (low aspect ratio) in low-speed streaks is high, and they are mostly trapped in low-speed streaks for a long time during the cyclic events mentioned. This mechanism is illustrated in Figure 60.

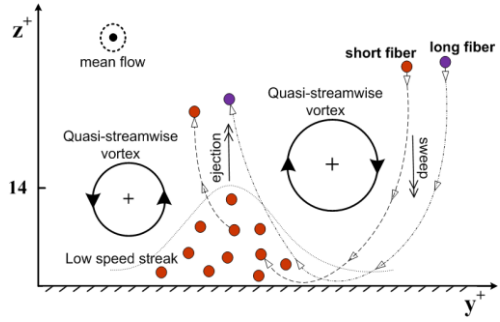

Figure 60 The mechanism predicted for fiber transfer and segregation;

The distribution of fluctuating wall-normal angular velocity of the fibers, $(\Omega_z')^+$, are shown in Figure 61. The mean wall-normal angular velocity is zero for all cases in all distances from the wall. Gaussian distribution function was fitted appropriately to the experimental data.

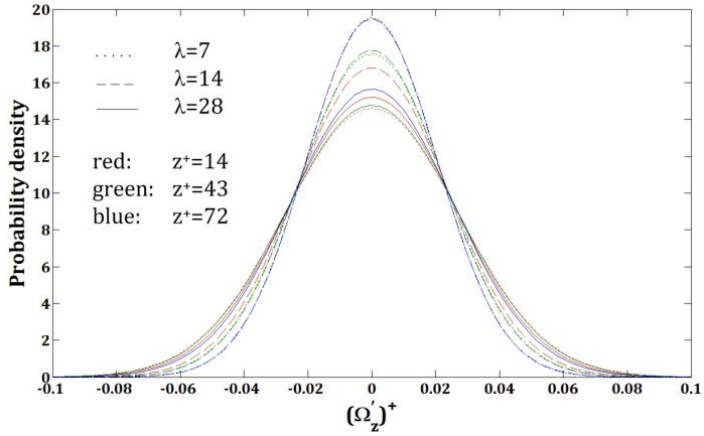

Figure 61 Probability density of fluctuating wall-normal angular velocity of the fiber, $(\Omega_z')^+$, for the different fiber sizes in the different wall-normal distance; the Gaussian PDF is fitted to the experimental data in a good manner;

This figure exhibits that PDF profiles of $(\Omega_z')^+$ for fibers in the middle sizes (λ=7 & 14) collapse on each other for distances far away from the wall (z^+=72 & 43). However, for long fiber (λ=28), it is different with a lower peak and higher and longer tails. This indicates some uncommon events for long fibers. Near the wall, the different behaviours are observed for the different sizes of fiber.

Chapter 7

CONCLUSION

1. A two-frame algorithm based on SOM neural network has been developed for matching rod-like particle pair that have one major symmetry axis for Fiber Tracking Velocimetry of fiber suspension flows. The evaluation of the algorithm has been established by means of synthetic particle images and DNS results of prolate-particle-laden turbulent channel flow. A major advantage of neural networks is that no initial knowledge of the flow area being examined and the particle behavior is needed. This feature makes neural networks attractive schemes for particle pairing. Moreover, for suspension flows involving rod-like particles tracking, the particle angle plays a key role in the matching of corresponding particles. Therefore, SOM neural network became the method chosen in the present study since it made us able to utilize all features of the particle images, i.e. both orientation and position, to find pair particles in relatively high-density particle images and establish a robust and reliable matching algorithm.

The test cases considered cover a wide range of applications. It was demonstrated that the tracking capability of the developed algorithm is superior for both high and low tracking parameter ϕ. In the case of homemade images of particles in a 2D potential flow in a corner, ϕ was varied from 1.75 to 0.87 by increasing the particle number density in the images. For ϕ>1.0, the ability of the algorithm to detect corresponding particles in successive image frames is excellent; η_r >83% and η_m<11%. The recovery ratio η_r is reduced to 64%, and the mismatch ratio η_r is raised to 30% for ϕ<1.0. The performance of the algorithm remains nevertheless satisfactorily. Furthermore, the elapsed time grows with the number of particles in the images and jumps to 2.1 s for ϕ<1.0. For data sets derived from the results of DNS-based computer simulations of prolate spheroidal particles in turbulent channel flow, the performance of the algorithm is evaluated for various values of ϕ with increasing time step between sequential image frames. For ϕ>1.0, the recovery ratio η_r exceeds 54%, and the mismatch ratio η_m is below 15%. The algorithm shows a weak performance for ϕ<1.0 because the low ϕ and the accompanying large time interval between samples cause a large variation in the orientation and position of particles. This makes particle tracking difficult.

Although the performance and reliability of the present algorithm has been demonstrated only for elongated rod-like particles in the present paper, we believe

that the same algorithm can be utilized also for suspensions of other non-spherical particles provided that the orientation of the individual particles can be defined for instance by means of an axis of symmetry.

2. It was found that the light scattering pattern from fibers in the light sheet depends on the incidence angle of the beam light and the viewing angle. This causes the variations of the fiber brightness level in images depends on their orientation. Therefore, it was introduced dynamic threshold concept to recognize the fibers reliably in the visualization volume. The dynamic threshold along with the matching algorithm proposed made us able to track correct fibers in consecutive image frames.

3. In addition, experimental study of behavior of rod-like stiff fibers dispersed in a wall-bounded turbulent flow has been carried out using PIV/PTV measurements. The suspension was a dilute mixture of cellulose acetate fibers with a diameter 70 μm in three different aspect ratios 7,14 & 28 and moderate response time (τ^+) in order of one into tap water. The friction Reynolds number was approximately 170, and the data are comparable with DNS results due to the inherent characteristic of the experimental setup.

In the present work, the motion and orientation statistics of fibers are reported to examine the fiber size effect and local flow structure on the behavior of long fibers (longer than local flow scales) in wall turbulence. It is well known that particle transfer mechanism is dominated by the near-wall turbulent coherent structures. The results we experimentally obtained reveal that the size of fiber is a significant factor for the dynamic behavior of fiber in the near-wall region. It was indicated that the probability of attendance of the long fibers (λ=28) is high in the ejection and sweep areas in the wall region. On the other hand, the results showed the short fibers accumulated likely into the low-speed area for a long time. In upper layers, the far-wall region, it was observed that almost all translational velocity statistics are negligibly affected by fiber aspect ratio.

Besides, it was found for long fibers near the wall that the high-speed fibers have no preferential orientation. This was not observed for short fibers. However, for all cases there is a high tendency of lower speed fibers to orientate in streamwise direction.

There is a significant difference in the behavior of fibers with lengths of 1 and 2 mm compared to the fibers with a length of 0.5 mm in the wall-normal distance of 1 mm (z^+=14). It is acceptable that the ratio of the fiber length to the fiber distance from the wall is an important parameter in the fiber behavior in the vicinity of a solid surface.

BIBLIOGRAPHY

[1] Crowe CT, Schwarzkopf JD, Sommerfeld M, Tsuji Y. "Multiphase Flows with Droplets and Particles": CRC press, 2011.

[2] Lundell F, Söderberg LD, Alfredsson PH."Fluid Mechanics of Papermaking".Annual Review of Fluid Mechanics 2011;43:195-217.

[3] Shinozaki M, Roberts KA, van de Goor B, Clyne TW."Deposition of Ingested Volcanic Ash on Surfaces in the Turbine of a Small Jet Engine".Advanced Engineering Materials 2013;15:986-94.

[4] Grindle TJ, Burcham FW."Engine Damage to a NASA Dc-8-72 Airplane from a High-Altitude Encounter with a Diffuse Volcanic Ash Cloud" 2003;NASA/TM-2003-212030.

[5] McDonough J. "Lectures on Turbulence", 2013.

[6] Jeong J, Hussain F, Schoppa W, Kim J."Coherent Structures near the Wall in a Turbulent Channel Flow".Journal of Fluid Mechanics 1997;332:185-214.

[7] Schoppa W, Hussain F."Coherent Structure Dynamics in near-Wall Turbulence".Fluid Dynamics Research 2000;26:119-39.

[8] Schoppa W, Hussain F."Coherent Structure Generation in near-Wall Turbulence".Journal of Fluid Mechanics 2002;453:57-108.

[9] Adrian R, Meinhart C, Tomkins C."Vortex Organization in the Outer Region of the Turbulent Boundary Layer".Journal of Fluid Mechanics 2000;422:1-54.

[10] Adrian RJ."Hairpin Vortex Organization in Wall Turbulence".Physics of Fluids 2007;19:041301.

[11] Maxey M."The Gravitational Settling of Aerosol Particles in Homogeneous Turbulence and Random Flow Fields".Journal of Fluid Mechanics 1987;174:441-65.

[12] Wang LP, Maxey MR."Settling Velocity and Concentration Distribution of Heavy-Particles in Homogeneous Isotropic Turbulence".Journal of Fluid Mechanics 1993;256:27-68.

[13] Elghobashi S, Truesdell GC."Direct Simulation of Particle Dispersion in a Decaying Isotropic Turbulence".Journal of Fluid Mechanics 1992;242:655-700.

[14] Eaton JK, Fessler JR."Preferential Concentration of Particles by Turbulence".International Journal of Multiphase Flow 1994;20:169-209.

[15] Balachandar S, Eaton JK."Turbulent Dispersed Multiphase Flow".Annual Review of Fluid Mechanics 2010;42:111-33.

[16] Tanaka T, Eaton JK."Sub-Kolmogorov Resolution Partical Image Velocimetry Measurements of Particle-Laden Forced Turbulence".Journal of Fluid Mechanics 2010;643:177.

[17] Shapiro M, Goldenberg M."Deposition of Glass-Fiber Particles from Turbulent Air-Flow in a Pipe".Journal of Aerosol Science 1993;24:65-87.

[18] Fan FG, Ahmadi G."A Sublayer Model for Wall Deposition of Ellipsoidal Particles in Turbulent Streams".Journal of Aerosol Science 1995;26:813-40.

[19] Newsom RK, Bruce CW."Orientational Properties of Fibrous Aerosols in Atmospheric Turbulence".Journal of Aerosol Science 1998;29:773-97.

[20] Olson JA."The Motion of Fibres in Turbulent Flow, Stochastic Simulation of Isotropic Homogeneous Turbulence".International Journal of Multiphase Flow 2001;27:2083-103.

[21] Zhang H, Ahmadi G, Fan F-G, McLaughlin JB."Ellipsoidal Particles Transport and Deposition in Turbulent Channel Flows".International Journal of Multiphase Flow 2001;27:971-1009.

[22] Moses KB, Advani SG, Reinhardt A."Investigation of Fiber Motion near Solid Boundaries in Simple Shear Flow".Rheologica Acta 2001;40:296-306.

[23] Paschkewitz JS, Dubief Y, Dimitropoulos CD, Shaqfeh ESG, Moin P."Numerical Simulation of Turbulent Drag Reduction Using Rigid Fibres".Journal of Fluid Mechanics 2004;518:281-317.

[24] Melander O, Rasmuson A."Piv Measurements of Velocities and Concentrations of Wood Fibres in Pneumatic Transport".Experiments in Fluids 2004;37:293-300.

[25] Xu H, Aidun CK."Characteristics of Fiber Suspension Flow in a Rectangular Channel".International Journal of Multiphase Flow 2005;31:318-36.

[26] Shin M, Koch DL."Rotational and Translational Dispersion of Fibres in Isotropic Turbulent Flows".Journal of Fluid Mechanics 2005;540:143-74.

[27] Parsheh M, Brown ML, Aidun CK."On the Orientation of Stiff Fibres Suspended in Turbulent Flow in a Planar Contraction".Journal of Fluid Mechanics 2005;545:245-69.

[28] Metzger B, Butler JE, Guazzelli EL."Experimental Investigation of the Instability of a Sedimenting Suspension of Fibres".Journal of Fluid Mechanics 2007;575:307-32.

[29] Mortensen P, Andersson H, Gillissen J, Boersma B."Dynamics of Prolate Ellipsoidal Particles in a Turbulent Channel Flow".Physics of fluids 2008;20:093302.

[30] Marchioli C, Fantoni M, Soldati A."Orientation, Distribution, and Deposition of Elongated, Inertial Fibers in Turbulent Channel Flow".Physics of Fluids 2010;22:033301.

[31] Andersson HI, Zhao L, Barri M."Torque-Coupling and Particle–Turbulence Interactions".Journal of Fluid Mechanics 2012;696:319-29.

[32] Do-Quang M, Amberg G, Brethouwer G, Johansson AV."Simulation of Finite-Size Fibers in Turbulent Channel Flows".Physical Review E 2014;89:013006.

[33] Bellani G, Byron ML, Collignon AG, Meyer CR, Variano EA."Shape Effects on Turbulent Modulation by Large Nearly Neutrally Buoyant Particles".Journal of Fluid Mechanics 2012;712:41-60.

[34] Hout R, Sabban L, Cohen A."The Use of High-Speed Piv and Holographic Cinematography in the Study of Fiber Suspension Flows".Acta Mech 2013;224:2263-80.

[35] Adrian RJ."Dynamic Ranges of Velocity and Spatial Resolution of Particle Image Velocimetry".Meas Sci Technol 1997;8:1393-8.

[36] Westerweel J."Efficient Detection of Spurious Vectors in Particle Image Velocimetry Data".Experiments in Fluids 1994;16:236-47.

[37] Westerweel J."Fundamentals of Digital Particle Image Velocimetry".Meas Sci Technol 1997;8:1379-92.

[38] Huang H, Dabiri D, Gharib M."On Errors of Digital Particle Image Velocimetry".Meas Sci Technol 1997;8:1427-40.

[39] Pereira F, Stüer H, Graff EC, Gharib M."Two-Frame 3d Particle Tracking".Measurement science and technology 2006;17:1680.

[40] Kobayashi T, Saga T, Segawa S."Multipoint Velocity Measurement for Unsteady Flow Field by Digital Image Processing".Flow Visualization V, Hemisphere 1989:197-202.

[41] Nishino K, Kasagi N, Hirata M."Three-Dimensional Particle Tracking Velocimetry Based on Automated Digital Image Processing".Journal of fluids engineering 1989;111:384-91.

[42] Hassan Y, Canaan R."Full-Field Bubbly Flow Velocity Measurements Using a Multiframe Particle Tracking Technique".Experiments in Fluids 1991;12:49-60.

[43] Malik NA, Dracos T, Papantoniou DA."Particle Tracking Velocimetry in Three-Dimensional Flows".Experiments in Fluids 1993;15:279-94.

[44] Okamoto K, Hassan Y, Schmidl W."New Tracking Algorithm for Particle Image Velocimetry".Experiments in Fluids 1995;19:342-7.

[45] Keane R, Adrian R, Zhang Y."Super-Resolution Particle Imaging Velocimetry".Measurement Science and Technology 1995;6:754.

[46] Cowen EA, Monismith SG."A Hybrid Digital Particle Tracking Velocimetry Technique".Experiments in Fluids 1997;22:199-211.

[47] Takehara K, Adrian R, Etoh G, Christensen K."A Kalman Tracker for Super-Resolution Piv".Experiments in Fluids 2000;29:S034-S41.

[48] Cardwell ND, Vlachos PP, Thole KA."A Multi-Parametric Particle-Pairing Algorithm for Particle Tracking in Single and Multiphase Flows".Measurement Science and Technology 2011;22:105406.

[49] Kaga A, Yamaguchi K, Kondo A, Inoue Y, Yamaguchi T, Kamoi S. "Flow Field Estimation Using Piv-Data and Fluid Dynamic Equations". Proc. PIV-Fukui'97, 1997. p.131-6.

[50] Baek S, Lee S."A New Two-Frame Particle Tracking Algorithm Using Match Probability".Experiments in Fluids 1996;22:23-32.

[51] Ohmi K, Li HY."Particle-Tracking Velocimetry with New Algorithms".Measurement Science and Technology 2000;11:603.

[52] Knaak M, Rothlubbers C, Orglmeister R. "A Hopfield Neural Network for Flow Field Computation Based on Particle Image Velocimetry/Particle Tracking Velocimetry Image Sequences". International Conference on Neural Networks, vol. 1, 1997. p.48-52 vol.1.

[53] Grant I, Pan X."The Use of Neural Techniques in Piv and Ptv".Measurement Science and Technology 1997;8:1399.

[54] Ohmi K, Sapkota A. "Particle Tracking Velocimetry Using Cellular Neural Network". International Joint Conference on Neural Networks (IJCNN), 2006. p.3963-9.

[55] Labonté G."A New Neural Network for Particle-Tracking Velocimetry".Experiments in Fluids 1999;26:340-6.

[56] Ohmi K."Som-Based Particle Matching Algorithm for 3d Particle Tracking Velocimetry".Applied Mathematics and Computation 2008;205:890-8.

[57] Ohmi K, Joshi B, Panday SP."A Som Based Stereo Pair Matching Algorithm for 3-D Particle Tracking Velocimetry".Lect Notes Artif Int 2009;5755:11-20.

[58] "Dantec Dynamics a/S, http://Www.Dantecdynamics.Com/".

[59] Delnoij E, Westerweel J, Deen NG, Kuipers JAM, van Swaaij WPM."Ensemble Correlation Piv Applied to Bubble Plumes Rising in a Bubble Column".Chemical Engineering Science 1999;54:5159-71.

[60] Kiger KT, Pan C."Piv Technique for the Simultaneous Measurement of Dilute Two-Phase Flows".J Fluid Eng-T Asme 2000;122:811-8.

[61] Gonzalez RC, Richard E. "Woods, Digital Image Processing", 2002.

[62] Carlsson A, Hakansson K, Kvick M, Lundell F, Soderberg LD."Evaluation of Steerable Filter for Detection of Fibers in Flowing Suspensions".Experiments in Fluids 2011;51:987-96.

[63] Fausett LV. "Fundamentals of Neural Networks: Architectures, Algorithms, and Applications": Prentice-Hall Englewood Cliffs, 1994.

[64] Ashforth-Frost S, Fontama VN, Jambunathan K, Hartle SL. "The Role of Neural Networks in Fluid Mechanics and Heat Transfer". Instrumentation and Measurement Technology Conference, 1995. IMTC/95. Proceedings. Integrating Intelligent Instrumentation and Control., IEEE, 1995. p.6.

[65] Faller WE, Schreck SJ."Unsteady Fluid Mechanics Applications of Neural Networks".Journal of aircraft 1997;34:48-55.

[66] Labonté G."Neural Network Reconstruction of Fluid Flows from Tracer-Particle Displacements".Experiments in Fluids 2001;30:399-409.

[67] Kohonen T."The Self-Organizing Map".Proceedings of the IEEE 1990;78:1464-80.

[68] Blair D, Dufresne E. "Particle Tracking Code in Matlab". http://physics.georgetown.edu/matlab/, 2008.

[69] Kvick M, Håkansson KO, Lundell F, Söderberg LD, Prahl Wittberg L."Streak Formation and Fibre Orientation in near Wall Turbulent Fibre Suspension Flow".ERCOFTAC bulletin 2010;84.

[70] Dean RB."Reynolds Number Dependence of Skin Friction and Other Bulk Flow Variable in Two-Dimensional Rectangular Duct Flow".Journal of Fluids Engineering 1978;100:215-23.

[71] Zanoun ES, Durst F, Nagib H."Evaluating the Law of the Wall in Two-Dimensional Fully Developed Turbulent Channel Flows".Physics of Fluids 2003;15:3079-89.

[72] Kawamura Lab. http://murasun.me.noda.tus.ac.jp/turbulence/index.html.

[73] Djalili-Moghaddam M, Toll S."Fibre Suspension Rheology: Effect of Concentration, Aspect Ratio and Fibre Size".Rheologica Acta 2006;45:315-20.

[74] Jacob M, Unser M."Design of Steerable Filters for Feature Detection Using Canny-Like Criteria". IEEE transactions on pattern analysis and machine intelligence 2004;26:1007-19.

[75] Cooke DD, Kerker M."Light Scattering from Long Thin Glass Cylinders at Oblique Incidence".J Opt Soc Am 1969;59:43-&.

[76] Cohen A, Acquista C."Light Scattering by Tilted Cylinders: Properties of Partial Wave Coefficients".JOSA 1982;72:531-4.

[77] Cohen LD, Haracz RD, Cohen A, Acquista C."Scattering of Light from Arbitrarily Oriented Finite Cylinders".Applied Optics 1983;22:742-8.

[78] Mees L, Ren KF, Grehan G, Gouesbet G."Scattering of a Gaussian Beam by an Infinite Cylinder with Arbitrary Location and Arbitrary Orientation: Numerical Results".Appl Opt 1999;38:1867-76.

[79] Lee Rodgers J, Nicewander WA."Thirteen Ways to Look at the Correlation Coefficient".The American Statistician 1988;42:59-66.

[80] Jeffery GB."The Motion of Ellipsoidal Particles Immersed in a Viscous Fluid".Proceedings of the Royal Society of London. Series A, Containing Papers of a Mathematical and Physical Character 1922;102:161-79.

[81] Marchioli C, Soldati A."Mechanisms for Particle Transfer and Segregation in a Turbulent Boundary Layer".Journal of fluid Mechanics 2002;468:283-315.

“ We've learned from experience that the truth will come out. Other experimenters will repeat your experiment and find out whether you were wrong or right. Nature's phenomena will agree or they'll disagree with your theory. And, although you may gain some temporary fame and excitement, you will not gain a good reputation as a scientist if you haven't tried to be very careful in this kind of work. And it's this type of integrity, this kind of care not to fool yourself, that is missing to a large extent in much of the research in cargo cult science. ”

Surely You're Joking, Mr. Feynman! ,

Richard Feynman